Dai *et al. Energy Mater* 2022;2:200040
DOI: 10.20517/energymater.2022.56

Energy Materials

Review

Open Access

Design of manganese dioxide for supercapacitors and zinc-ion batteries: similarities and differences

Henghan Dai[1,#], Ruicong Zhou[1,#], Zhao Zhang[2,#], Jinyuan Zhou[3,*], Gengzhi Sun[1,*]

[1]School of Flexible Electronics (Future Technologies), Nanjing Technology University, Nanjing 211816, Jiangsu, China.
[2]College of Intelligent Science and Control Engineering, Jinling Institute of Technology, Nanjing 211169, Jiangsu, China.
[3]School of Physical Science and Technology, Lanzhou University, Lanzhou 730000, Gansu, China.
[#]Authors contributed equally.

[*]**Correspondence to:** Prof./Dr. Jinyuan Zhou, School of Physical Science and Technology, Lanzhou University, 222 Tianshui South Road, Lanzhou 730000, Gansu, China. E-mail: zhoujy@lzu.edu.cn; Prof./Dr. Gengzhi Sun, School of Flexible Electronics (Future Technologies), Nanjing Technology University, 5 Xin Mofan Road, Nanjing 211816, Jiangsu, China. E-mail: iamgzsun@njtech.edu.cn

How to cite this article: Dai H, Zhou R, Zhang Z, Zhou J, Sun G. Design of manganese dioxide for supercapacitors and zinc-ion batteries: similarities and differences. *Energy Mater* 2022;2:200040. https://dx.doi.org/10.20517/energymater.2022.56

Received: 22 Sep 2022 **First Decision:** 26 Oct 2022 **Revised:** 16 Nov 2022 **Accepted:** 29 Nov 2022 **Published:** 12 Dec 2022

Academic Editors: Yuping Wu, Bin Wang **Copy Editor:** Ke-Cui Yang **Production Editor:** Ke-Cui Yang

Abstract

Energy storage devices, e.g., supercapacitors (SCs) and zinc-ion batteries (ZIBs), based on aqueous electrolytes, have the advantages of rapid ion diffusion, environmental benignness, high safety and low cost. Generally, SCs provide excellent power density with the capability of fast charge/discharge, while ZIBs offer high energy density by storing more charge per unit weight/volume. Although the charge storage mechanisms are considered different, manganese dioxide (MnO_2) has proven to be an appropriate electrode material for both SCs and ZIBs because of its unique characteristics, including polymorphic forms, tunable structures and designable morphologies. Herein, the design of MnO_2-based materials for SCs and ZIBs is comprehensively reviewed. In particular, we compare the similarities and differences in utilizing MnO_2-based materials as active materials for SCs and ZIBs by highlighting their corresponding charge storage mechanisms. We then introduce a few commonly adopted strategies for tuning the physicochemical properties of MnO_2 and their specific merits. Finally, we discuss the future perspectives of MnO_2 for SC and ZIB applications regarding the investigation of charge storage mechanisms, materials design and the enhancement of electrochemical performance.

Keywords: Aqueous energy storage devices, manganese dioxide, zinc-ion batteries, supercapacitors, mechanisms

© The Author(s) 2022. **Open Access** This article is licensed under a Creative Commons Attribution 4.0 International License (https://creativecommons.org/licenses/by/4.0/), which permits unrestricted use, sharing, adaptation, distribution and reproduction in any medium or format, for any purpose, even commercially, as long as you give appropriate credit to the original author(s) and the source, provide a link to the Creative Commons license, and indicate if changes were made.

INTRODUCTION

In recent decades, electrochemical energy storage devices have been widely applied as power systems for a variety of applications ranging from portable electronics and electric vehicles to smart electric grids[1-5]. Due to their advantages of high energy density and long cycling lifespan without a memory effect, lithium-ion batteries (LIBs) are the most successful products, with the 2019 Nobel Prize in Chemistry awarded to John B. Goodenough, M. Stanley Whittingham and Akira Yoshino[6-11]. However, safety issues, such as fires and explosions, are always major concerns regarding the utilization of LIBs since their lithium salt-containing organic electrolytes are highly flammable[12-15]. To address this issue, one viable strategy is to develop aqueous-based devices, which are considered as promising alternatives due to their high safety and low cost[16-22].

Presently, two types of aqueous-based devices, namely, supercapacitors (SCs) and zinc-ion batteries (ZIBs), as schematically illustrated in Figure 1A and B, have attracted tremendous attention owing to their unique features[20,23-29]. Typically, SCs exhibit ultralong cyclic stability, fast charge/discharge rates and high power density, thus explaining their broad applications in urban public transportation, aerospace, the military, and so on[30-33]. The charges are stored in SC materials based on two mechanisms: (1) adsorption/desorption of electrolyte ions on the electrode surface, excluding any redox reactions (electrochemical double-layer capacitance, EDLC); and (2) fast and reversible redox reactions on the electrode materials (pseudocapacitance). In contrast, ZIBs are considered promising candidates for grid-scale safe energy storage due to their low redox potential (-0.76 V *vs.* NHE), high theoretical capacity (820 mAh g^{-1}) due to the metal Zn anode, intrinsic nonflammability, non-toxicity and high ionic conductivity of the aqueous electrolytes and low cost[34-38].

In contrast to SCs, electrolyte ions (Zn^{2+}) are inserted and extracted from the electrode materials, usually accompanied with phase transitions. Undoubtedly, the performance of both devices severely relies on their electrode materials[39-41]. Based on the statistics summarized in Figure 1C and D, it is very interesting to find that the commonly used electrode materials for SCs, including nanocarbon, conducting polymers, transition metal oxides (RuO_2 and MnO_2), transition metal dichalcogenides (TMDs) and transition metal carbides/nitrides (MXenes), are also suitable for ZIBs. Among these materials, the most studied one is manganese dioxide (MnO_2) because of its natural abundance, non-toxicity, wide potential window and high theoretical capacitance/capacity[42-47]. For example, α-MnO_2 nanoneedles synthesized by a microwave-assisted method were used as SC materials and delivered 289 F g^{-1} at 0.5 A g^{-1} in 1 M Na_2SO_4 and maintained 88% after cycling 10,000 times[48]. A δ-MnO_2-based cathode for ZIBs showed a capacity of 200 mAh g^{-1} at 0.1 A g^{-1} after full electrochemical activation[49]. However, when utilized as electrode materials for SCs and ZIBs, MnO_2 typically faces similar problems, including high electrical resistance, cycling instability, slow electrode kinetics, and so on. Moreover, the charge storage mechanisms of MnO_2 in SCs and ZIBs are still under debate. In particular, based on the literature, complicated processes are involved when MnO_2 is applied in ZIBs, whereas pseudocapacitive behavior is understood in SCs. Although several articles have been published summarizing the applications of MnO_2 either in SCs or ZIBs, a comprehensive and comparative review to elucidate the similarity and difference in materials design for both devices is essential[50-53]. Herein, we focus on the recent advances in the design and utilization of MnO_2 in aqueous-based SCs and ZIBs. In particular, we describe the respective charge storage mechanisms, highlight the materials design principles and provide a direct comparison and perspectives for future endeavors regarding MnO_2-based SCs and ZIBs.

CRYSTAL STRUCTURE

The commonly utilized MnO_2 polymorphs in SCs and ZIBs can be classified into α-MnO_2, β-MnO_2,

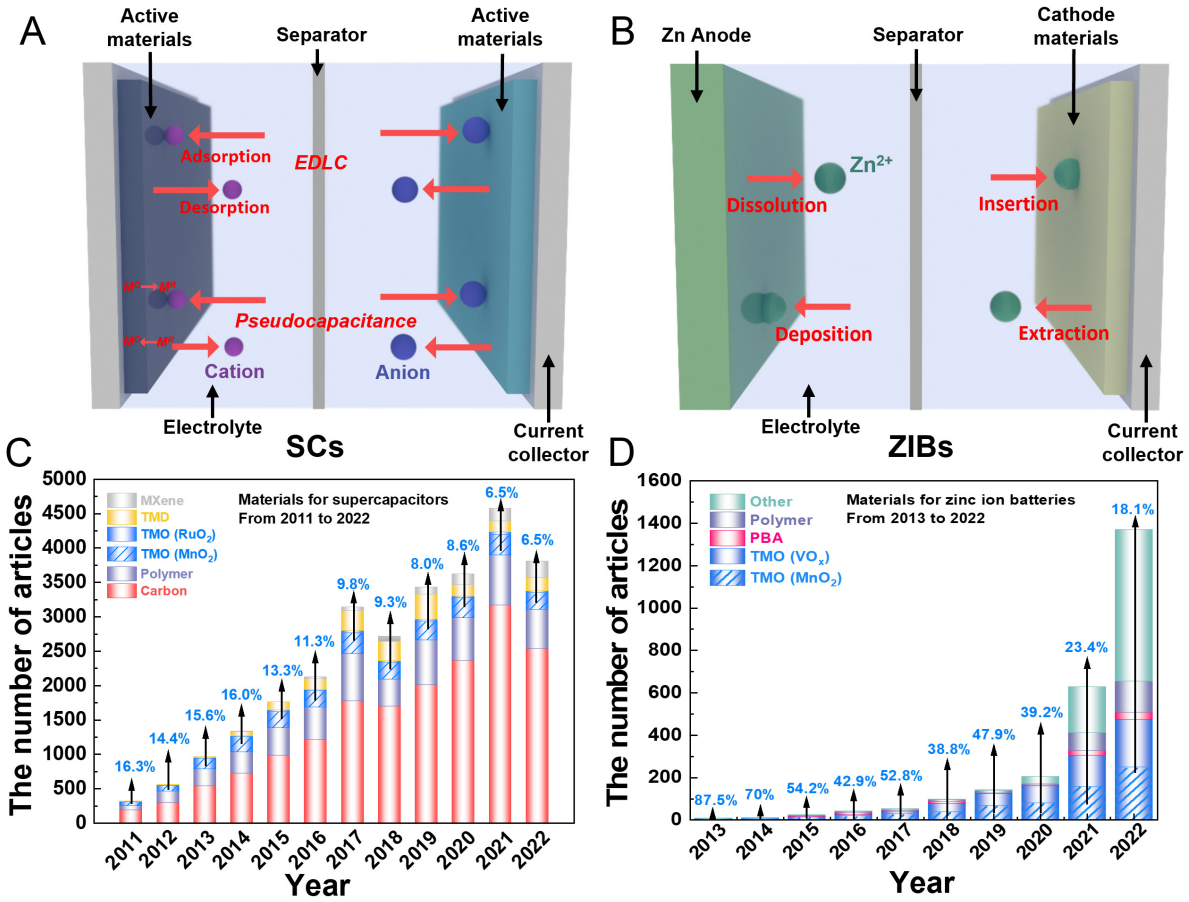

Figure 1. Schematic illustrations of (A) SC and (B) ZIB devices. (C) publication numbers of different materials, including MXenes, TMDs, carbon, polymers and TMOs (MnO_2 and RuO_2), for SCs in the period from 2011 to 2022. (D) publication numbers of different cathode materials, such as TMOs (VO_x and MnO_2), PBAs, polymers and other materials (including carbonaceous materials, TMDs and MXenes), for ZIBs in the period from 2013 to 2022. All data were obtained from the Web of Science. EDLC: electrochemical double-layer capacitance; SCs: supercapacitors; ZIBs: zinc-ion batteries.

δ-MnO_2, γ-MnO_2 and amorphous MnO_2 [Figure 2] by arranging the MnO_6 octahedral units either *via* edge-sharing, corner-sharing or a combination of two[26]. In particular, in α-MnO_2 [Figure 2A], MnO_6 octahedral double chains are connected in a corner-sharing manner to form 2 × 2 tunnels (4.6 × 4.6 Å). In β-MnO_2 [Figure 2B], single chains assembled by MnO_6 octahedra are interlinked in a corner-sharing manner to form 1 × 1 tunnels (2.3 × 2.3 Å). In γ-MnO_2, both 1 × 1 and 1 × 2 tunnels coexist and distribute randomly [Figure 2C]. Alternatively, in δ-MnO_2, two-dimensional (2D) sheets are built by sharing MnO_6 octahedral edges [Figure 2D] and then stacked into laminar structures with an interlayer spacing of ~7 Å[23]. It is known that the intercalated cations or water molecules between the sheets play a critical role in stabilizing the layered structure[54]. In comparison, amorphous MnO_2 possesses a highly disordered structure [Figure 2E] with higher strength, lower hardness, larger surface area and even superior structural stability[55,56].

SUPERCAPACITORS

Charge storage mechanisms

MnO_2 is considered a pseudocapacitive material[57]. Traditionally, it is believed that the capacitance of MnO_2 originates from surface redox reactions with a theoretical value of ~110 μF cm^{-2} based on a

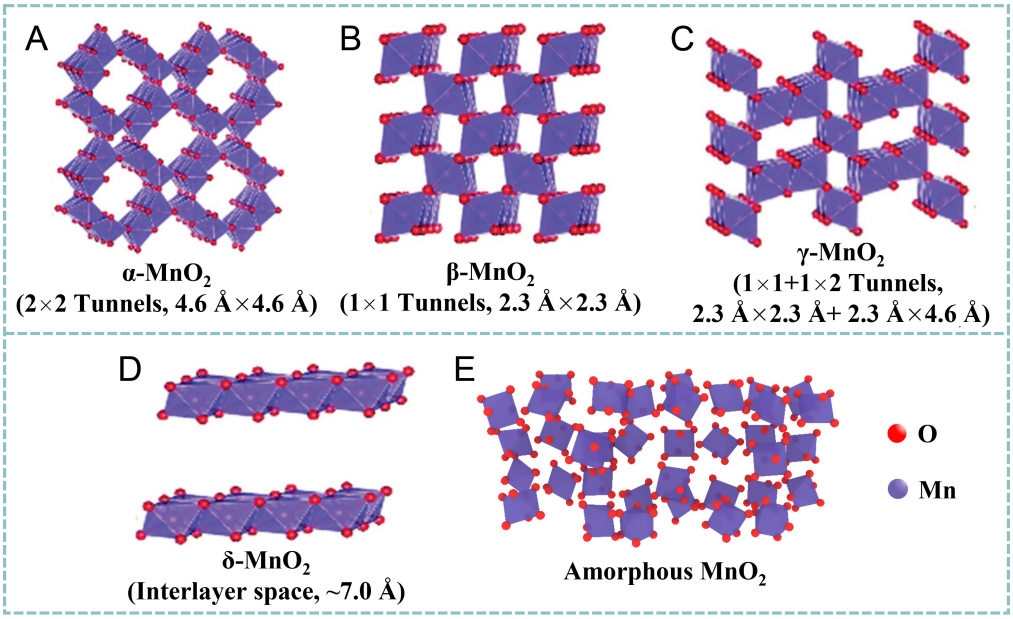

Figure 2. Crystal structures of (A) α-, (B) β-, (C) γ-, (D) δ- and (E) amorphous MnO_2. Reproduced with permission[26]. Copyright 2019, Royal Society of Chemistry.

Brunauer-Emmett-Teller surface (10 to 180 m^2 g^{-1})[58]. Nevertheless, a much higher capacitance (over 300 F g^{-1}) was obtained experimentally in a neutral electrolyte, suggesting extra contributions from other electrochemical mechanisms beyond the surface redox reactions[59]. Zhang *et al.* confirmed the capacitance from the insertion/extraction of Na^+ in δ-MnO_2 by assembling a sodium-ion capacitor [Figure 3A][60]. The interlayer spacing of layered δ-MnO_2 was expanded to ~7 Å after activation during the first discharge. Moreover, the contribution of diffusion-controlled capacitance was determined to be as high as 64.4% of the total charge storage at 0.1 mV s^{-1} (0-1.2 V *vs.* SCE), indicating that the dominant charge storage depends on Na^+ insertion/extraction. In another work, Chen *et al.* investigated the charge storage mechanism of Zn^{2+} pre-intercalated α-MnO_2 (Zn_xMnO_2) nanowires in a blended aqueous electrolyte (2 M $ZnSO_4$ and 0.4 M $MnSO_4$)[61]. *Ex-situ* Inductive Coupled Plasma (ICP) analysis showed that the Zn/Mn molar ratio in Zn_xMnO_2 varied from 0.029 to 0.596 during the first three discharge processes, corresponding to the reversible insertion/extraction of Zn^{2+} [Figure 3B]. The reaction mechanism follows Equation (1):

$$Zn_xMnO_2 - 2(x-y)e^- \leftrightarrow Zn_yMnO_2 + (x-y)Zn^{2+} \quad (1)$$

The electrochemical behavior of MnO_2 is found to be heavily dependent on the pH of the electrolyte [Figure 3C][62,63]. In a neutral electrolyte, the generated Mn^{3+} ions involve a slow process of disproportionation following Equation (2), leading to Mn^{2+} loss and continuous capacity decay[64,65]. Furthermore, MnO_2 structures experience volume expansion, thereby loosening the electrical contacts between MnO_2 particles, increasing the series resistance and lowering the capacitance over time[66,67]. These issues compromise the power density and cycle life of MnO_2 directly[63,68]. In an acidic electrolyte, except for the redox reaction between H^+ and MnO_2, excessive H^+ induces the further reduction of MnOOH to Mn^{2+}, leading to the irreversible dissolution of MnO_2 Equations (3) and (4)[63]. In an alkaline electrolyte, hydroxyl ions (OH^-) react with MnO_2 at the surface, generating a layer of insulative $Mn(OH)_2$, which prevents the inner active materials from being exposed to the electrolyte ions. The overall electrochemical reactions in an alkaline electrolyte follow Equations (5)-(9) with a narrow voltage window of < 0.7 V[69].

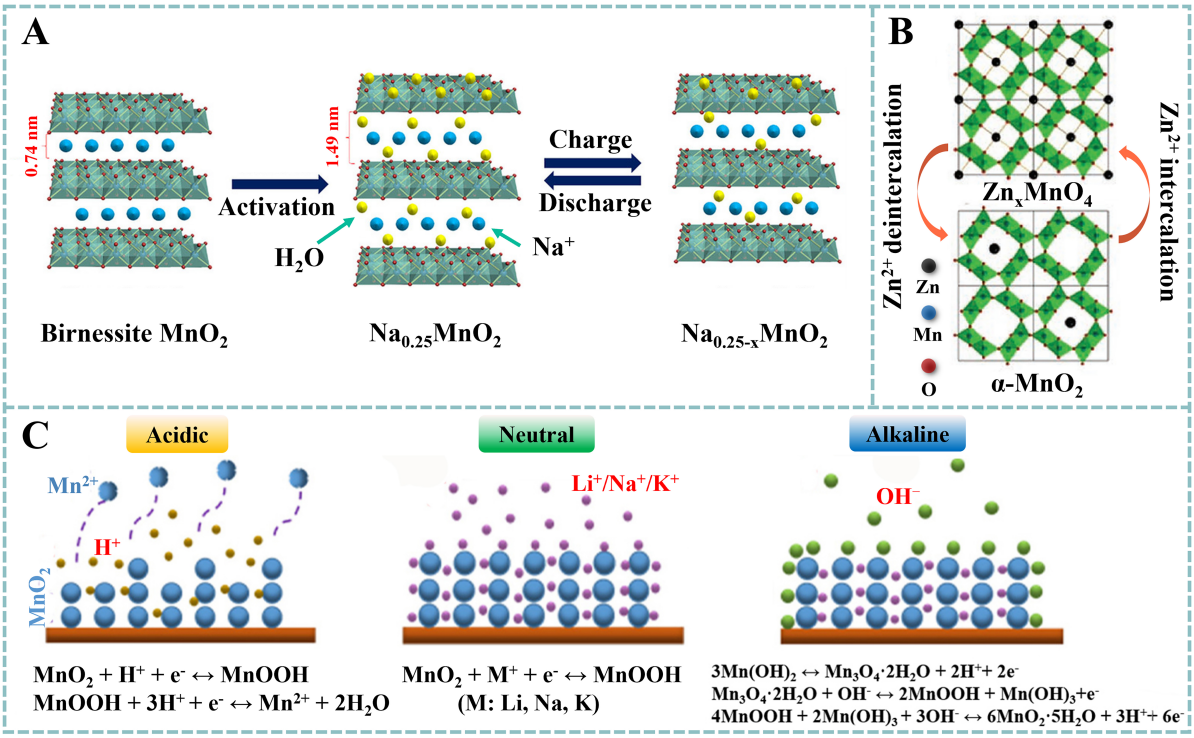

Figure 3. (A) Intercalation/deintercalation of Na^+ using $NaClO_4$ as the electrolyte. Reproduced with permission[60]. Copyright 2018, Elsevier. (B) charge storage mechanism of α-MnO_2-based SC using $ZnSO_4$ and $MnSO_4$ as the electrolyte. Reproduced with permission[61]. Copyright 2020, Wiley-VCH. (C) redox reactions of MnO_2 in acidic, neutral and alkaline electrolytes, respectively. Reproduced with permission[63]. Copyright 2019, Elsevier.

In a neutral electrolyte:

$$2Mn^{3+} \leftrightarrow Mn^{4+} + Mn^{2+}(aq) \quad (2)$$

In an acidic electrolyte:

$$MnO_2 + H^+ + e^- \rightarrow MnOOH \quad (3)$$

$$MnOOH + 3H^+ + e^- \rightarrow Mn^{2+}(aq) + 2H_2O \quad (4)$$

In an alkaline electrolyte:

$$MnO_2 + H_2O + e^- \rightarrow MnOOH + OH^- \quad (5)$$

$$MnOOH + H_2O + e^- \rightarrow Mn(OH)_2 + OH^- \quad (6)$$

$$3Mn(OH)_2 \leftrightarrow Mn_3O_4{\cdot}2H_2O + 2H^+ + 2e^- \quad (7)$$

$$Mn_3O_4{\cdot}2H_2O + OH^- \leftrightarrow 2MnOOH + Mn(OH)_3 + e^- \quad (8)$$

$$4MnOOH + 2Mn(OH)_3 + 6OH^- \leftrightarrow 6MnO_2{\cdot}5H_2O + 3H_2O + 6e^- \quad (9)$$

Overall, two main charge storage mechanisms are involved for MnO_2 when adopted in aqueous SCs: (i) surface redox reactions Equation (10); and (ii) intercalation/deintercalation of cations Equation (11):

$$(MnO_2)_{surface} + M^+ + e^- \leftrightarrow (MnOOM)_{surface} \quad (10)$$

$$(MnO_2)_{bulk} + M^+ + e^- \leftrightarrow (MnOOM)_{bulk} \quad (11)$$

Performance enhancements

Nanostructure design

Enhancing the ion diffusion kinetics *via* nanostructural design is considered a feasible method to improve the capacitance of MnO_2[70-77]. Xiong *et al.* prepared interlayer expanded MnO_2 (0.93 nm) with intercalated tetramethylammonium ions (TMA^+), following a two-step cation exchange [Figure 4A][78]. Density functional theory (DFT) calculations suggested that the expanded interlayer can weaken the interactions between the negatively charged MnO_2 and K^+ due to the decreased diffusion energy barrier, thereby accelerating ion diffusion during charge/discharge. A specific capacitance of 160 F g^{-1} was obtained for the restacked MnO_2 in aqueous K_2SO_4 electrolytes at 0.2 A g^{-1}, while at 10 A g^{-1}, 70% capacitance was retained (110 F g^{-1}). In contrast, in the cases of K- and H-MnO_2 nanobelts, only 50% and 55% capacitance retentions were obtained, respectively, as the current density increased from 0.2 to 10 A g^{-1} [Figure 4B]. Moreover, the long-term cycling performance of the restacked MnO_2 nanosheets was evaluated at 5 A g^{-1} for 5000 cycles with 100% retention.

Foreign ion/molecular pre-insertion

Since the charge storage capacity of MnO_2 can be enhanced by the Mn^{4+}/Mn^{3+} redox pair with cation adsorption (or intercalation)[79-81], it is speculated that the pre-insertion of cations in MnO_2 could improve the specific capacitance by enhancing ion diffusion[81-83]. Following this guidance, Jabeen *et al.* prepared birnessite $Na_{0.5}MnO_2$ arrays on a carbon cloth by the electrochemical conversion of Mn_3O_4 in 10 M Na_2SO_4 *via* cyclic scanning at 10 mV s^{-1} within the potential window of 0 and 1.3 V (*vs.* Ag/AgCl) for 500 cycles [Figure 4C][84]. The incorporation of Na^+ not only upgraded the specific capacitance but also widened the workable potential window to 1.3 V. The redox reaction of the Mn^{3+}/Mn^{4+} couple was verified by *ex-situ* X-ray photoelectron spectroscopy, while the newly emerged peaks at 0.96 V were attributed to the insertion and extraction of residual Na^+. The obtained $Na_{0.5}MnO_2$ electrode showed an obviously improved capacitance of 366 F g^{-1} without compromising its cycling stability [Figure 4D]. Asymmetric SCs were constructed using $Na_{0.5}MnO_2$ and Fe_3O_4 as the cathode and anode, respectively. The asymmetric SC using 1 M Na_2SO_4 as the electrolyte exhibited a cell voltage of 2.6 V, a capacitance of 88 F g^{-1} and an energy density of 81 Wh kg^{-1}.

Defect engineering

In addition to ion diffusion, the high electrical resistance of MnO_2 needs to be lowered to achieve rapid electron transport during the redox reactions[85-87]. Defect engineering (heteroatom doping and the introduction of oxygen vacancies) has been demonstrated to be an effective strategy for improving the conductivity of MnO_2[88-96]. Kang *et al.* designed a thick Au-doped MnO_2 film (1.35 μm) by electrochemically depositing MnO_2 and sputtering Au alternately to adjust the electronic structure of MnO_2 [Figure 5A][97]. Au atoms distributed in the lattice of MnO_2 with a total doping level of 9.9 at.% act as electron donors to induce a new state in the bandgap (~1.0 eV), thereby enhancing the overall conductivity, which is beneficial to the kinetics of the electrode reaction [Figure 5B]. As shown in Figure 5C, the specific capacitance of the

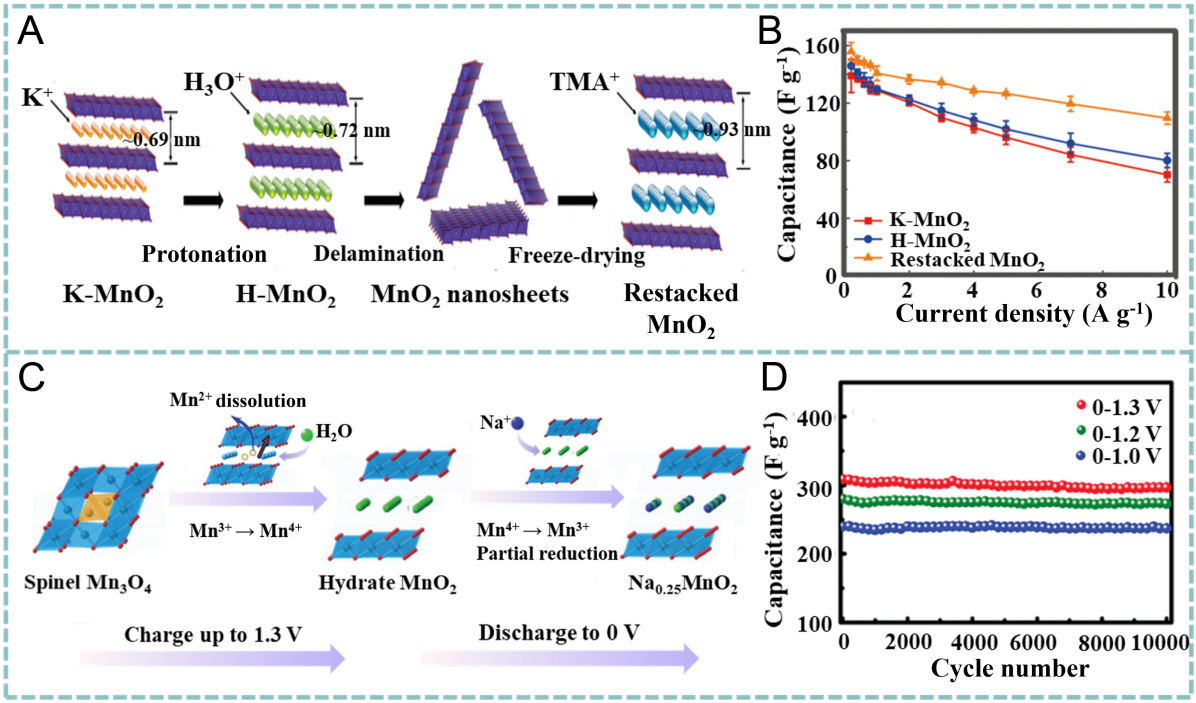

Figure 4. (A) Synthetic process of restacked MnO_2. (B) rate capability in K_2SO_4 electrolyte at current densities from 0.2 to 10 A g^{-1}. Reproduced with permission[78]. Copyright 2017, American Chemical Society. (C) structural evolution of Mn_3O_4 during electrochemical oxidation. (D) cyclic performance of $Na_{0.5}MnO_2$ nanowall arrays (NWAs) in different potential windows. Reproduced with permission[84]. Copyright 2017, Wiley-VCH.

Au-doped MnO_2 is much higher than that of pristine MnO_2 (2.5 eV). With increasing Au-doping level, the specific capacitance first increases and then decreases slightly. As a result, the Au-doped MnO_2 film achieved a gravimetric capacitance (C_g) as high as 626 F g^{-1} tested in 2 M Li_2SO_4 at 5 mV s^{-1} and superior stability over 15000 charge/discharge cycles [Figure 5D]. In addition, substituting Mn with heterogeneous atoms (such as Co, Ni, Al, Fe, Ag and Au) in MnO_2 tends to change the electronic structure of MnO_2 *via* electron donation. For example, Wang *et al.* synthesized a series of interlinked Fe-doped MnO_2 nanostructures *via* a hydrothermal method[98]. It was confirmed that the incorporation of Fe atoms effectively prevented the collapse of MnO_2 crystals during protonation, thereby prolonging the service life of the device. The optimized sample with a mass loading of ~5 mg cm^{-2} exhibited a specific capacitance of 267.0 F g^{-1} at 0.1 A g^{-1} with 68.6% retention at 1 A g^{-1} and excellent cycling stability over 2000 cycles at 2 A g^{-1} (~100% retention).

Alternatively, Peng *et al.* hydrothermally built an oxygen vacancy-rich MnO_{2-x}/reduced graphene oxide (rGO) composite in tetrahydrofuran using manganese carbonyl ($Mn(CO)_5$) and GO as the precursors[99]. Benefiting from the good electronic conduction in the interconnected rGO networks and high redox activity of the partially reduced MnO_2 nanoparticles, the vacancy-rich MnO_{2-x}/rGO film showed a high specific capacitance of 675.5 F g^{-1} (0.5 A g^{-1}) in a 0.5 mol L^{-1} Na_2SO_4 solution and retained 96.1% of the capacitance after 10,000 cycles. Amorphous MnO_2 with abundant vacancies and ion transport channels has also been considered as a promising electrode material for SCs. As a typical work, Shi *et al.* fabricated hybrid fiber electrodes by anchoring amorphous MnO_2 on well-aligned multiwall carbon nanotube (MWCNT) sheets, followed by twisting [Figure 5E][100]. The MWCNT sheets, which were drawn from a spinnable array, showed excellent electron conductivity that facilitated the redox reaction of amorphous MnO_2. The direct

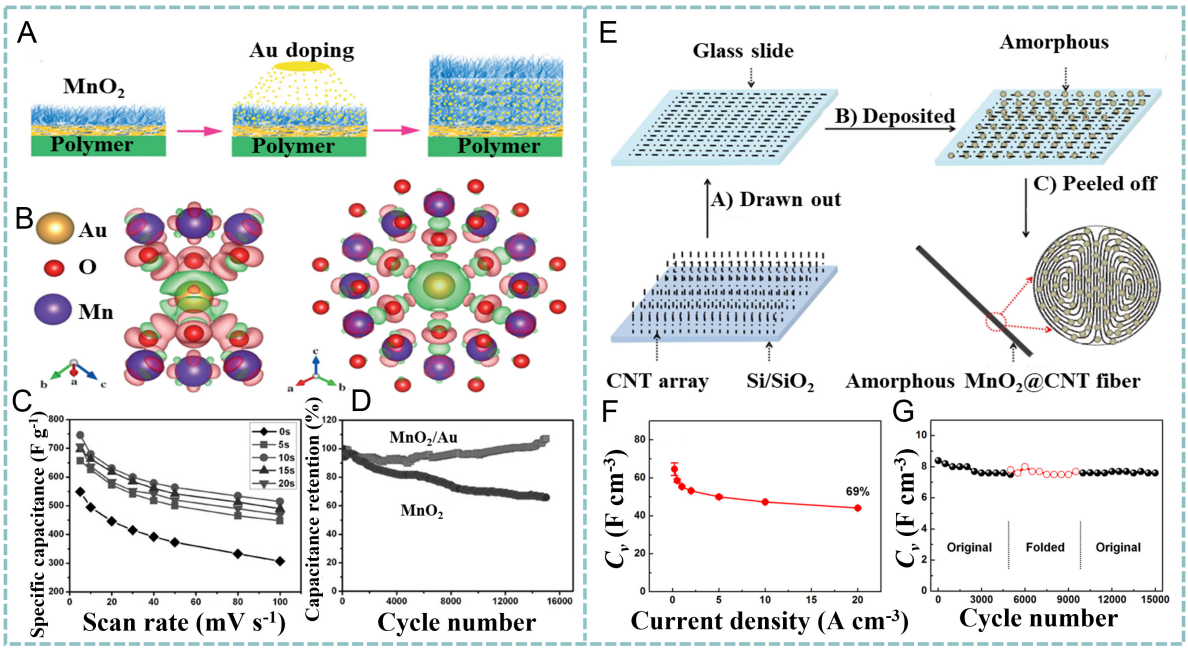

Figure 5. (A) Fabrication and (B) first-principle calculations of Au-doped MnO_2. Differential charge densities of (left) Au-substituted and (right) Au-interstitial MnO_2. Green indicates a loss of electrons and pink represents a gain of electrons. (C) specific capacitance of Au/MnO_2 at different Au sputtering times. (D) cycling stability of pure MnO_2 and Au-doped MnO_2 electrodes with the same thickness of ~1.35 μm. Reproduced with permission[97]. Copyright 2013, Wiley-VCH. (E) fabrication of amorphous MnO_2@MWCNT fibers. (F) *CV* of amorphous MnO_2@MWCNT fiber electrode. (G) cycling and bending stability of fiber SC at 1 A cm^{-3}. Reproduced with permission[100]. Copyright 2017, American Chemical Society.

chemical deposition of amorphous MnO_2 was carried out at 80 °C using acidic $KMnO_4$ and MWCNTs as the precursors *via* Equations (12) and (13):

$$4MnO_4^- + 3C + H_2O \rightarrow 4MnO_2 + CO_3^{2-} + 2HCO_3^- \quad (12)$$

$$4MnO_4^- + 4H^+ \rightarrow 4MnO_2 + 3O_2 + 2H_2O \quad (13)$$

Benefiting from the abundant ion transport channels and the fast electron transport of the MWCNTs, the as-prepared amorphous MnO_2@MWCNT fibers exhibited a capacitance of 60.8 F cm^{-3} at 0.2 A cm^{-3} with the calculated contribution of MnO_2 as high as 615.2 F g^{-1} and excellent rate performance retaining 44.1 F cm^{-3} at 20 A cm^{-3} [Figure 5F]. The symmetric SC made of amorphous MnO_2@MWCNT fibers delivered a volumetric capacitance (C_V) of 10.9 F cm^{-3} at 0.1 A cm^{-3} and retained 6.9 F cm^{-3} at 5 A cm^{-3}, together with an E_V of 1.5 mWh cm^{-3} at the P_V of 0.05 W cm^{-3}. In addition, the fiber SC also presented outstanding stability over 15,000 charge/discharge cycles and mechanical robustness for 5000 bending/unbending cycles [Figure 5G].

Hybridization

Combining the merits of two materials *via* hybridization is highly desired for improving the performance of MnO_2[101-104]. Zhu *et al.* developed a core-shell structure by depositing δ-MnO_2 nanosheets on the outer surface of β-MnO_2 *via* two-step hydrothermal reactions using MnOOH nanowires as the self-sacrificial template and $KMnO_4$ as the oxidant [Figure 6A][105]. It was found from their experiments that the content of Mn^{3+} played a critical role in improving the electrical conductivity of MnO_2 due to the double-exchange

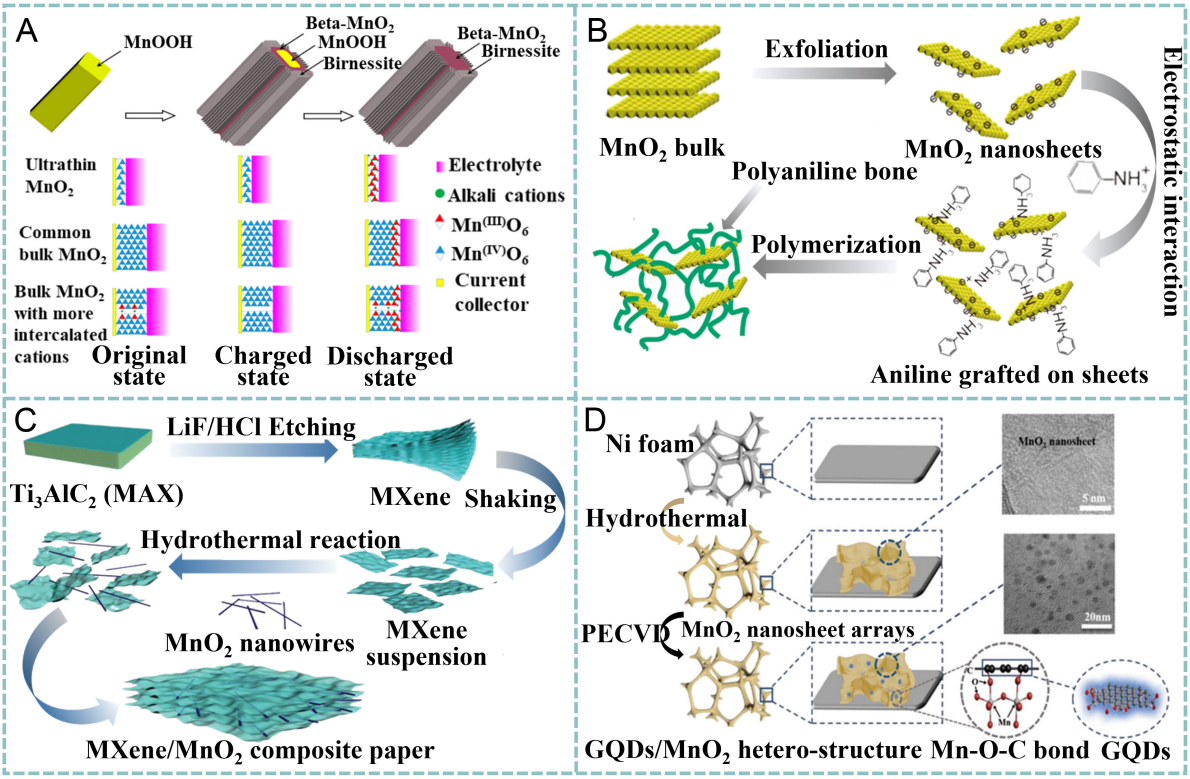

Figure 6. (A) Synthesis of β-MnO_2/parallel birnessite core/shell nanorod and a diagram illustrating the enhanced utilization of Mn. Reproduced with permission[105]. Copyright 2018, American Chemical Society. (B) preparation of 3D network composed of MnO_2 sheets and PANI chains. Reproduced with permission[106]. Copyright 2017, American Chemical Society. (C) fabrication of Ti_3C_2Tx/MnO_2 NW composite paper. Reproduced with permission[107]. Copyright 2018, Wiley-VCH. (D) fabrication of GQD/MnO_2 heterostructures. Reproduced with permission[113]. Copyright 2018, Wiley-VCH. GQDs: graphene quantum dots.

interaction forming Mn^{3+}-O-Mn^{4+}. The as-prepared MnO_2 with a Mn^{3+}/Mn^{4+} ratio of 0.69 exhibited a C_g of 306 F g^{-1} at 0.25 A g^{-1}, retaining 226 F g^{-1} at 64 A g^{-1} and 207 F g^{-1} after cycling at 2 A g^{-1} for 3000 times. Liu *et al.* prepared a three-dimensional (3D) mesoporous architecture composed of MnO_2/polyaniline (PANI) networks *via* the top-down exfoliation of δ-MnO_2, the electrostatic attraction between the MnO_2 nanosheets and aniline monomer and the chemical polymerization in the presence of $(NH_4)_2S_2O_8$ [Figure 6B][106]. The hybrid exhibited a high conductivity of 0.08 S cm^{-1}, which was slightly lower than that of neat PANI (0.09 S cm^{-1}), due to the electrical interconnections formed by PANI. The as-obtained MnO_2/PANI composite presented a high C_g of 762 F g^{-1} at 1 A g^{-1}, retaining 587 F g^{-1} at 10 A g^{-1} and 578 F g^{-1} at 5 A g^{-1} over 8000 charge/discharge cycles.

Recently, a hybrid paper electrode with high flexibility was proposed by Zhou *et al.* through vacuum infiltrating a homogeneous suspension of MXene ($Ti_3C_2T_x$) nanosheets and MnO_2 nanowires [Figure 6C][107]. The high conductivity of the 2D MXene sheets (over 8000 S cm^{-1}) facilitated the electron transport of MnO_2 during charge/discharge and prevented the aggregation of MnO_2, thus ensuring the accessibility of the electrolyte ions. The optimized performance was obtained with a $Ti_3C_2T_x/MnO_2$ mass ratio of six, delivering a C_a (areal capacitance) of 205 mF cm^{-2} (corresponding to a C_V of 1025 F cm^{-3}), 98% retention after cycling at 0.2 mA cm^{-2} for 10000 times and good bending/unbending robustness. Carbonaceous materials were also adopted to improve the electrochemical performance of MnO_2 electrodes[89,108-112]. Jia *et al.* reported that graphene quantum dots (GQDs) were adopted using a plasma

enhanced chemical vapor deposition process for the modification of MnO_2 nanosheets *via* Mn-O-C bonds [Figure 6D][113]. An electric field was generated at the interface between the GQDs (~5.2 eV) and MnO_2 (~4.4 eV) owing to their different work functions, thereby providing a barrier for electronic transmission and enabling the extraction of free electrons from MnO_2 and the subsequent accumulation at the edges of the GQDs until the Fermi levels were aligned. Consequently, the MnO_2/GQD heterostructures demonstrated an expanded potential window of 1.3 V (*vs.* $Hg/HgCl_2$) in 1 M Na_2SO_4, a C_g of 1170 F g^{-1} at 5 mV s^{-1} and good stability with 92.7% capacitance retained after 10,000 cycles.

ZINC-ION BATTERIES

Charge storage mechanisms

Distinct from those described for SCs above, the charge storage mechanisms of MnO_2 in aqueous ZIBs are relatively complicated, possibly involving the insertion/extraction of Zn^{2+}, the co-insertion/extraction of H^+ and Zn^{2+} and the reversible dissolution-deposition of MnO_2/Mn^{2+}[50]. Typically, although MnO_2 with tunnel structures that can accommodate Zn^{2+}, such as α-MnO_2 (2 × 2 tunnels), β-MnO_2 (1 × 1 tunnels) and γ-MnO_2 (1 × 2 and 1 × 1 tunnels), are considered as promising cathodes for ZIBs, they suffer from irreversible phase conversions to layered structure, spinel structure ($ZnMn_2O_4$) or both during discharge/charge, as shown in Figure 7A[114,115]. Alfaruqi *et al.* reported the application of a hydrothermally synthesized α-MnO_2 cathode for rechargeable ZIBs using a $ZnSO_4$ aqueous solution as the electrolyte within a cell voltage of 1.0-1.8 V[116]. X-ray diffraction (XRD) and *ex-situ* synchrotron X-ray absorption spectroscopy measurements confirmed the reversible insertion and extraction of Zn^{2+} accompanied by the formation and decomposition of $ZnMn_2O_4$. Alternatively, Lee *et al.* proposed a reversible and electrochemically triggered phase conversion between α-MnO_2 and layered Zn-birnessite (or Zn-buserite) upon the intercalation/deintercalation of Zn^{2+}[117]. The phase conversion mechanism during Zn^{2+} insertion was ascribed to the partial dissolution of MnO_2 in the electrolyte because of the Jahn-Teller effect. With the insertion of Zn^{2+}, Mn^{4+} is reduced to Mn^{3+} Equation (14) and the gray bridge-like double chains of the $Mn^{3+}O_6$ units are gradually destroyed because of Mn^{2+} dissolution Equation (15), thereby forming a Zn-birnessite structure. Upon recharging, the dissolved Mn^{2+} can intercalate back and bridge the layers to tunnels with α-MnO_2 completely recovered Equation (16)[114]:

$$Mn^{4+}(s) + e^- \rightarrow Mn^{3+}(s) \quad (14)$$

$$2Mn^{3+}(s) \rightarrow Mn^{4+}(s) + Mn^{2+}(aq) \quad (15)$$

$$Mn^{2+}(aq) \rightarrow Mn^{4+}(s) + 2e^- \quad (16)$$

Distinctly, using *ex-situ* and synchrotron XRD and *in-situ* X-ray absorption near edge structure, Alfaruqi *et al.* unveiled that orthorhombic γ-MnO_2 underwent a phase transformation upon the insertion of Zn^{2+} [Figure 7B] following Equations (17) and (18)[118]. During discharge, the oxidation state of Mn in γ-MnO_2 was reduced from Mn^{4+} to Mn^{3+}/Mn^{2+}, accompanied with a structural transformation from an orthorhombic Mn^{4+} phase to a spinel-type Mn^{3+} phase ($ZnMn_2O_4$) and two intermediary soluble Mn^{2+} phases, namely, γ-Zn_xMnO_2 (tunnel type) and L-$ZnyMnO_2$ (layered type), as a result of the electrochemical Zn intercalation [Figure 7C]. In fact, γ-MnO_2 is composed of R-MnO_2 (ramsdellite) and β-MnO_2 (pyrolusite) phases in a slightly distorted hcp array of the oxygen anion sublattice. In contrast, the $ZnMn_2O_4$ and L-Zn_yMnO_2 phases share a cubic close-packing (ccp) array of the oxygen network. The intercalation of Zn^{2+} in γ-MnO_2 led to an anisotropic expansion of the orthorhombic unit cell, transforming the hcp oxygen sublattice to a ccp structure[119]. It was noted that a small hump corresponding to the high intensity line of the spinel-type $ZnMn_2O_4$ phase (2θ of ~32°) appeared to be retained even after complete charging. This

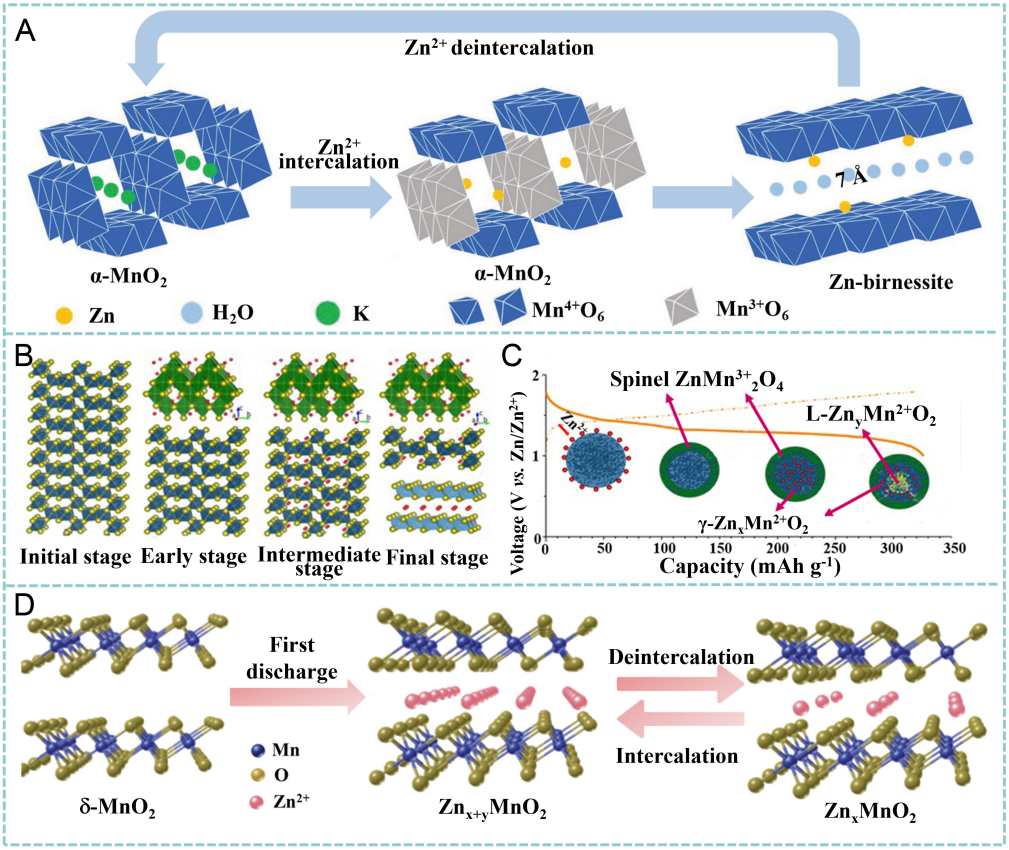

Figure 7. (A) Phase transition between Zn-birnessite and α-MnO_2. Reproduced with permission[114]. Copyright 2018, Wiley-VCH. (B and C) reaction pathway of Zn insertion in prepared γ-MnO_2 cathode. Reproduced with permission[118]. Copyright 2015, American Chemical Society. (D) Zn^{2+} intercalation/deintercalation mechanism for orthorhombic MnO_2. Reproduced with permission[120]. Copyright 2021, Royal Society of Chemistry.

behavior clearly suggests that the spinel phase may not completely revert to the orthorhombic phase and most likely may contribute to some of the capacity loss observed during extended cycling.

$$Zn^{2+} + 2e^- + 2MnO_2 \rightarrow Zn_2MnO_4 \quad (17)$$

$$nZn^{2+} + 2xe^- + MnO_2 \rightarrow Zn_nMnO_2 \quad (18)$$

δ-MnO_2 with a typical layered structure has also been directly utilized as a cathode material for ZIBs. Li *et al.* investigated the electrochemical storage mechanism of a -MnO_2 cathode using *ex-situ* XRD, scanning electron microscopy (SEM) and X-ray photoelectron spectroscopy[120]. The results, as schematically shown in Figure 7D, indicated that at the first discharge stage, birnessite $Zn_{x+y}MnO_2$ was formed during the intercalation of Zn^{2+} into -MnO_2 and then some Zn^{2+} ions were retained in the MnO_2 interlayer channel (Zn_xMnO_2) in the subsequent charge/discharge. Therefore, the storage behavior was described as the interlayer diffusion of Zn^{2+} without any observations regarding the changes in crystal structure.

The co-intercalation of H^+ and Zn^{2+} is also an important mechanism for MnO_2 cathodes in ZIBs. Liu *et al.* investigated the charge storage process of tunnel-structured MnO_2 nanotubes pre-intercalated by K^+ (α-$K_{0.19}MnO_2$) in 3 M $Zn(CF_3SO_3)_2$ and 0.2 M $Mn(CF_3SO_3)_2$[121]. It was found that α-$K_{0.19}MnO_2$ underwent

chemical conversion and cation interaction, as schematically shown in Figure 8A. The *ex-situ* XRD results demonstrated the reversible formation/decomposition of the Zn-buserite phase during the insertion/extraction of H^+ and Zn^{2+} [Figure 8B and C], corresponding to the two platforms in the discharge/charge curve. Liu *et al.* studied the phase evolution of β-MnO_2 upon electrochemical charge/discharge in 3 M $ZnSO_4$ and 0.2 M $MnSO_4$[122]. *Ex-situ* XRD suggested that the intercalation of H^+ retained the crystal structure of β-MnO_2 with the formation of $Zn_2(OH)_2(SO_4)(H_2O)_4$, while the subsequent insertion of Zn^{2+} resulted in a partial phase transformation to spinel $ZnMn_2O_4$ [Figure 8D]. Taking the evidence from high-resolution transmission electron microscopy (HRTEM) and TEM [Figure 8E] into consideration, it was concluded that the irreversible formation of $ZnMn_2O_4$ after long-term cycling resulted in capacity fade for the β-MnO_2 cathode. Li *et al.* revealed the storage mechanism of birnessite-type MnO_2 in 2.0 M $ZnSO_4$ and 0.5 M $MnSO_4$ [Figure 8F][123]. When discharged from 1.9 to 1.5 V, the H^+ intercalation reaction produced MnOOH Equation (19). Subsequently, with further discharge to 1.41 V, the Zn^{2+} insertion reaction Equation (20) led to the formation of $Zn_2Mn_4O_8{\cdot}H_2O$. Finally, MnOOH and $Zn_2Mn_4O_8{\cdot}H_2O$ completely converted into Mn^{2+} and $Zn_4SO_4(OH)_6{\cdot}5H_2O$ with a Mn^{4+}/Mn^{2+} two-electron pathway achieved Equations (21) and (22):

$$MnO_2 + H^+ + e \rightarrow MnOOH \tag{19}$$

$$4MnO_2 + 2Zn^{2+} + 4e + H_2O \rightarrow Zn_2Mn_4O_8{\cdot}H_2O \tag{20}$$

$$2MnOOH + SO_4^{\ 2} + 4Zn^{2+} + 7H_2O + 2e \rightarrow Zn_4SO_4(OH)_6{\cdot}5H_2O + 2Mn^{2+} \tag{21}$$

$$3Zn_2Mn_4O_8{\cdot}H_2O + 8SO_4^{\ 2} + 61H_2O + 26Zn^{2+} + 12e \rightarrow 8Zn_4SO_4(OH)_6{\cdot}5H_2O + 12Mn^{2+} \tag{22}$$

In contrast, Jin *et al.* unveiled the successive intercalation of Zn^{2+} and H^+, respectively, corresponding to the high and low voltage plateaus by exploring the electrochemical behavior of δ-MnO_2 in a $Zn(TFSI)_2$-based aqueous electrolyte[124]. Bulky $TFSI^-$ (*vs.* SO_4^{2-}) can decrease the number of water molecules surrounding the Zn^{2+} cation and reduce the solvation effect, thus facilitating Zn^{2+} transport and charge transfer. Therefore, in the $Zn(TFSI)_2$-based electrolyte, the non-diffusion-controlled mechanism dominates the first step of fast Zn^{2+} storage in bulk δ-MnO_2 without a significant phase transition Equation (23), while the diffusion-controlled conversion reaction between H^+ and MnO_2 dominates the following step reactions Equations (24)-(26):

$$MnO_2 + xZn^{2+} + 2xe^- \leftrightarrow Zn_xMnO_2 \text{ (non-diffusion controlled)} \tag{23}$$

$$H_2O \leftrightarrow H^+ + OH^- \tag{24}$$

$$MnO_2 + H^+ + e^- \leftrightarrow MnOOH \text{ (diffusion controlled)} \tag{25}$$

$$3Zn^{2+} + 6OH^- + Zn(TFSI)_2 + xH_2O \leftrightarrow Zn(TFSI)_2[Zn(OH)_2]_3{\cdot}xH_2O \tag{26}$$

Typically, the dissolution of Mn^{2+} and the generation/decomposition of $Zn_4SO_4(OH)_6{\cdot}H_2O$ (ZSH) observed in $ZnSO_4$ electrolytes are regarded as side reactions for capacity fade. However, a recent study performed by Guo *et al.* proposed a dissolution-deposition mechanism in a Zn//MnO_2 battery Equations (27)-(30) and confirmed the capacity contribution from the reversibly formed ZSH[125]. As shown in Figure 8G, α-MnO_2 (or -MnO_2) reacted with H_2O to produce ZSH and Mn^{2+} in the first discharge process and then ZSH reacted with Mn^{2+} to form birnessite-MnO_2 in the first charge process. Such a dissolution-deposition mechanism

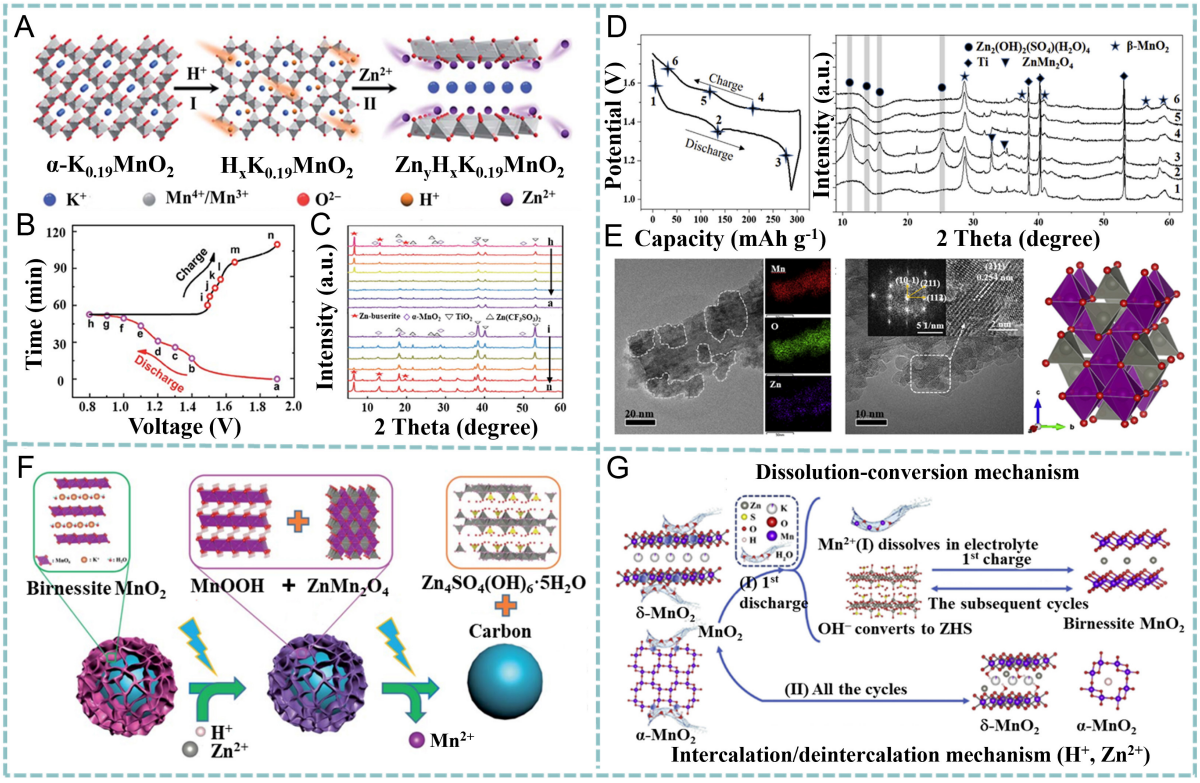

Figure 8. (A) Co-intercalation of Zn^{2+} and H^+ in α-$K_{0.19}MnO_2$. (B) voltage-time profile at 1 C and (C) corresponding XRD patterns (*ex situ*) of α-$K_{0.19}MnO_2$ during second discharge/charge cycle. The electrolyte contains $Zn(CF_3SO_3)_2$ (3 M) and $Mn(CF_3SO_3)_2$ (0.2 M). Reproduced with permission[121]. Copyright 2019, Royal Society of Chemistry. (D) GCD profile and corresponding XRD patterns (*ex situ*) of β-MnO_2 at 0.05 C, suggesting the insertion/extraction of H^+. (E) TEM/HRTEM observations of β-MnO_2 nanofiber and schematic crystal structure (hetaerolite). Reproduced with permission[122]. Copyright 2019, Elsevier. (F) sequential insertion of H^+ and Zn^{2+} during discharge process. Reproduced with permission[123]. Copyright 2020, Royal Society of Chemistry. (G) charge storage mechanism of MnO_2 cathode involving dissolution-deposition process. Reproduced with permission[125]. Copyright 2020, Elsevier.

dominated the subsequent energy storage processes, with the newly formed birnessite-MnO_2 as a host material contributing most of the specific capacity. In contrast, the intercalation/deintercalation of H^+/Zn^{2+} in residual undissolved MnO_2 is considered to contribute negligible capacity.

$$3MnO_2 + 6H_2O + 6e^- \rightarrow 3Mn^{2+} + 12OH^- \quad (27)$$

$$3Mn^{2+} + 12OH^-\ 6e^- \rightarrow 3\text{birnessite-}MnO_2 + 6H_2O \quad (28)$$

$$3\text{birnessite-}MnO_2 + 6H_2O + 6e^- \leftrightarrow 3Mn^{2+} + 12OH^- \quad (29)$$

$$12OH^- + 2SO_4^{2-} + 8Zn^{2+} + 8H_2O \leftrightarrow 2Zn_4(OH)_6SO_4{\cdot}4H_2O \quad (30)$$

Performance enhancements

Foreign ion/molecular pre-insertion

One of the current issues for the development of Mn-based cathodes is the sluggish reaction kinetics caused by a high-energy barrier for Zn^{2+} migration due to the strong electrostatic interactions with the host material, as well as the serious structural transformation during cycling[64]. The incorporation of cations (e.g., K^+, Na^+, Zn^{2+} and Ca^{2+}) in MnO_2 *via* surface coordination has been proven to be an effective strategy for

accelerating ion diffusion in tunnels or interlayer corridors, improving electrical conductivity and stabilizing the host structures[61,121,126,127]. Fang *et al.* synthesized potassium manganate ($K_{0.8}Mn_8O_{16}$, KMO) nanorods *via* the intercalation of K^+ into the tunnel cavities and used them as cathode materials for ZIBs[128]. It is reported that the steadily intercalated K^+ *via* the K-O bonds in the tunnels of KMO can effectively suppress the dissolution of Mn [Figure 9A]. As a result, the KMO-based ZIB exhibited a capacity of over 300 mAh g^{-1} at 100 mA g^{-1}, an energy density of 398 Wh kg^{-1} (based on the mass of the cathode) and impressive durability over 1000 cycles at 1 A g^{-1} (154 mAh g^{-1}). In contrast, pristine α-MnO_2 exhibited a significant capacity fade with only 50 mAh g^{-1} after 200 cycles. Anions (e.g., PO_4^{3}) can also be inserted into host materials, leading to structural defects, narrow bandgaps and enhanced electrical conductivity[129]. Zhang *et al.* employed crosslinked vertical multilayer graphene (VMG) arrays as the skeleton for the uniform growth of MnO_2 nanosheets[130]. The obtained MnO_2@VMG shell/core arrays were subsequently phosphorized under an Ar flow at 200 °C in the presence of $NaH_2PO_2 \cdot H_2O$ to form P-MnO_{2-x}@VMG [Figure 9B]. It was found that the phosphorization induced the intercalation of PO_4^{3-} and oxygen defects in MnO_2 simultaneously and expanded the interlayer spacing of (001) (from 0.68 to 0.70 nm), which facilitated ion transfer. The obtained P-MnO_{2-x}@VMG cathode exhibited enhanced electrochemical performance in an aqueous electrolyte of 2 M $ZnSO_4$ and 0.2 M $MnSO_4$, delivering a capacity of 302.8 mAh g^{-1} at 0.5 A g^{-1}, a high energy density of 369.5 Wh kg^{-1} and > 90% capacity retention after 1000 cycles at 2.0 A g^{-1}. In comparison, MnO_2@VMG provided 261.1 mAh g^{-1} at 0.5 A g^{-1} and 79.4% capacity retention after 1000 cycles at 2.0 A g^{-1}.

Alternatively, Huang *et al.* prepared mesoporous PANI-intercalated MnO_2 nanosheets with a thickness of ~10 nm and expanded interlayer space of ~1.0 nm through the polymerization at the interface of the organic and aqueous phases [Figure 9C][131]. The oxidation-induced polymerization of aniline (in CCl_4) and the reduction of MnO_4^{2-} (in H_2O) occurred simultaneously, thereby restricting the growth of MnO_2 anisotropically and facilitating the layer-by-layer assembly of the 2D MnO_2 and PANI. Since the guest polymer in the interlayer of the MnO_2 nanosheets efficiently prevented phase transformation and strengthened the layered structure during repeated insertion/extraction of hydrated cations, a reversible discharge capacity of 280 mAh g^{-1} at 200 mA g^{-1} was achieved with 110 mAh g^{-1} retained even at 3 A g^{-1}. Compared to its monovalent counterparts, Zn^{2+} requires high energy for desolvation at the electrode-electrolyte interface, thereby imposing an additional energy penalty for its facile intercalation[132]. In addition, the strong electrostatic interaction between Zn^{2+} and the host frameworks leads to the sluggish diffusion of Zn^{2+}[82]. Nam *et al.* demonstrated that the interlayer crystal water can effectively screen the electrostatic interactions between Zn^{2+} and the host, thus facilitating Zn^{2+} diffusion[54]. Layered MnO_2 containing crystal water in the interlayer space (cw-MnO_2) was prepared through electrochemical transformation from spinel-Mn_3O_4 in a 1 M $MgSO_4$ solution because the insertion of H_3O^+ is far more favorable over Mg^{2+}. DFT calculations revealed that Zn^{2+} prefers octahedrally coordinated triple-corner-sharing (TCS) sites with three H_2O molecules by forming a tridentate bond with a Zn-Mn dumbbell structure [Figure 9D]. Therefore, upon intercalation, Zn^{2+} ions tend to migrate together with the coordinate water molecules because of the strong Zn-H_2O coordination bond, which effectively weakens the electrostatic interaction between Zn^{2+} and MnO_2. As a result, cw-MnO_2 exhibited high reversible capacities of 350 mAh g^{-1} at 100 mA g^{-1}, 154 mAh g^{-1} at 3 A g^{-1} and 116 mAh g^{-1} after 200 cycles at 3 A g^{-1}. A similar observation was reported by Wang *et al.*, where H_2O molecules not only stabilize the intercalated Na^+ in the structure ($Na_{0.44}Mn_2O_4 \cdot 1.5H_2O$) but also promote the intercalation of Zn^{2+} during discharge in ZIBs[133].

Defect engineering

Defect engineering is another widely adopted method to enhance the performance of MnO_2 by tuning the electronic structure, enhancing the structural robustness and adjusting the interaction between the host and Zn^{2+}[134,135]. Oxygen vacancies (V_O) have proven their capability in gauging the adsorption/desorption of

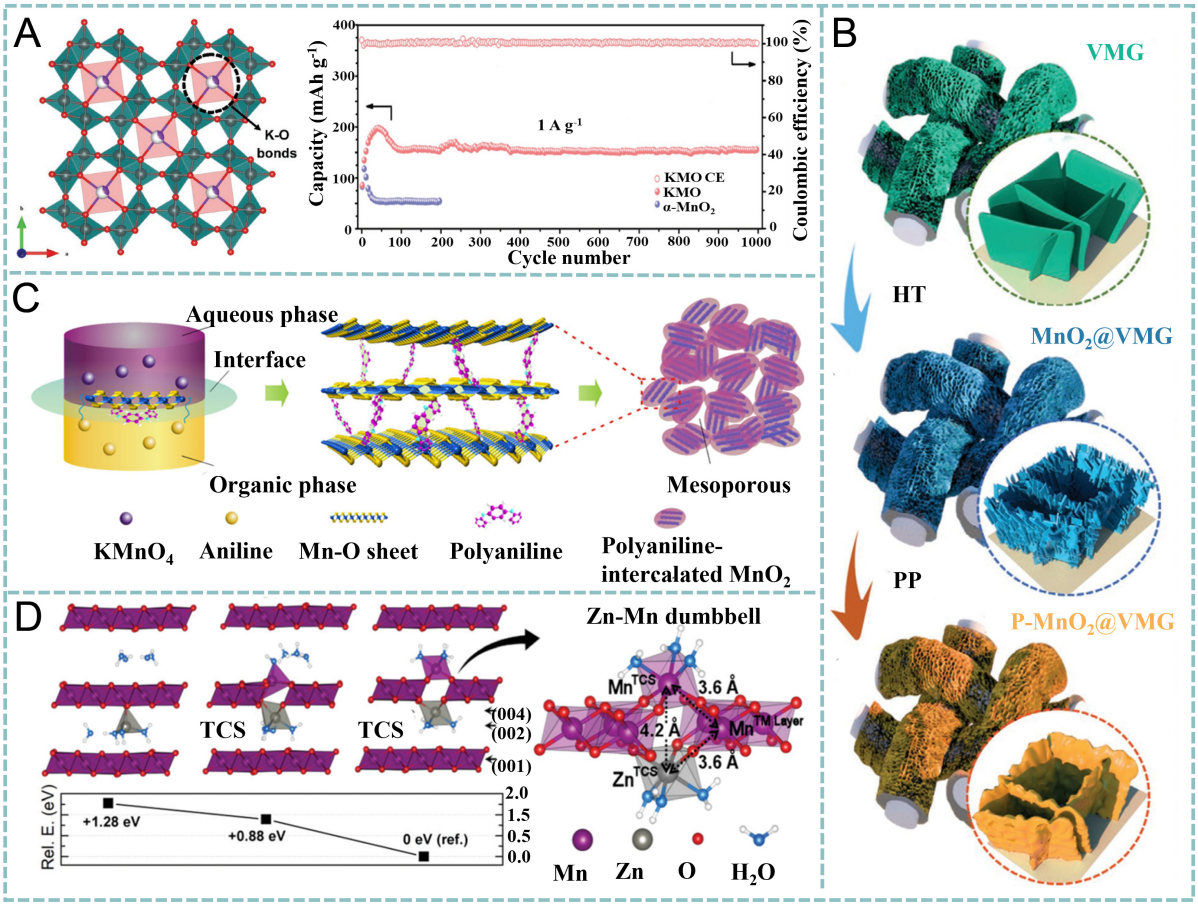

Figure 9. (A) Tunnel structure stabilized by K^+ and cycling performance of KMO and α-MnO_2 at 1 A g^{-1}. Reproduced with permission[128]. Copyright 2019, Wiley-VCH. (B) synthesis of P-MnO_{2-x}@VMG shell/core arrays. Reproduced with permission[130]. Copyright 2020, Wiley-VCH. (C) preparation and structural advantage of PANI-intercalated MnO_2 nanolayers. Reproduced with permission[131]. Copyright 2018, Nature. (D) optimized structure of cw-MnO_2 for Zn^{2+} intercalation and the corresponding relative energies. Reproduced with permission[54]. Copyright 2019, Royal Society of Chemistry. HT: hydrothermal method; TCS: triple-corner-sharing; KMO: $K_{0.8}Mn_8O_{16}$; PP: phosphorization; VMG: vertical multilayer graphene.

Zn^{2+}[93]. For example, Xiong *et al.* proposed the use of oxygen-deficient δ-MnO_2 (V_O-MnO_2) as cathode materials for ZIBs[136]. The storage mechanisms of Zn^{2+} in V_O-MnO_2 involve the insertion/extraction of Zn^{2+} into the interlayer spacing, surface redox reaction of $xZn^{2+} + 2xe^- + MnO_2 \rightarrow MnOOZn_x$ and the formation of electric double layers [Figure 10A]. The calculated Gibbs free energies of Zn^{2+} adsorption at the vicinity sites to V_O are close to thermoneutral values of ~0.05 eV [Figure 10B], suggesting a weakened bonding strength between Zn and O due to the diminished charge transfer. Therefore, more reversible adsorption/desorption of Zn^{2+} can be achieved for V_O-MnO_2 rather than pristine MnO_2. As a result, V_O-MnO_2 in an aqueous electrolyte of 1 M $ZnSO_4$ and 0.2 M $MnSO_4$ delivered a specific capacity of 345 mAh g^{-1} without any decay after 100 cycles at 0.2 A g^{-1} [Figure 10C]. The Zn-ion storage capability of MnO_2 can also be improved by heteroatom doping[137]. Zhao *et al.* hydrothermally synthesized Ni-doped MnO_2 with a stoichiometry of $Ni_{0.052}K_{0.119}Mn_{0.948}O_2$-$0.208H_2O$ (NKMO)[138]. The reference sample prepared without $Ni(NO_3)_2$ was KMO. The presence of the Ni-induced tetragonal-orthorhombic lattice distortion can mediate the cooperative motion of H^+ *via* the formation of hydrogen bonds similar to Grotthuss proton hopping in water [Figure 10D]. The electrochemical performance of NKMO and KMO cathodes was evaluated using a Zn plate as an anode in a 3 M $ZnSO_4$ and 0.2 M $MnSO_4$ aqueous electrolyte. The discharge capacity of the Zn/NKMO cell was ~303 mAh g^{-1}, which was ~29% higher than that of Zn/KMO

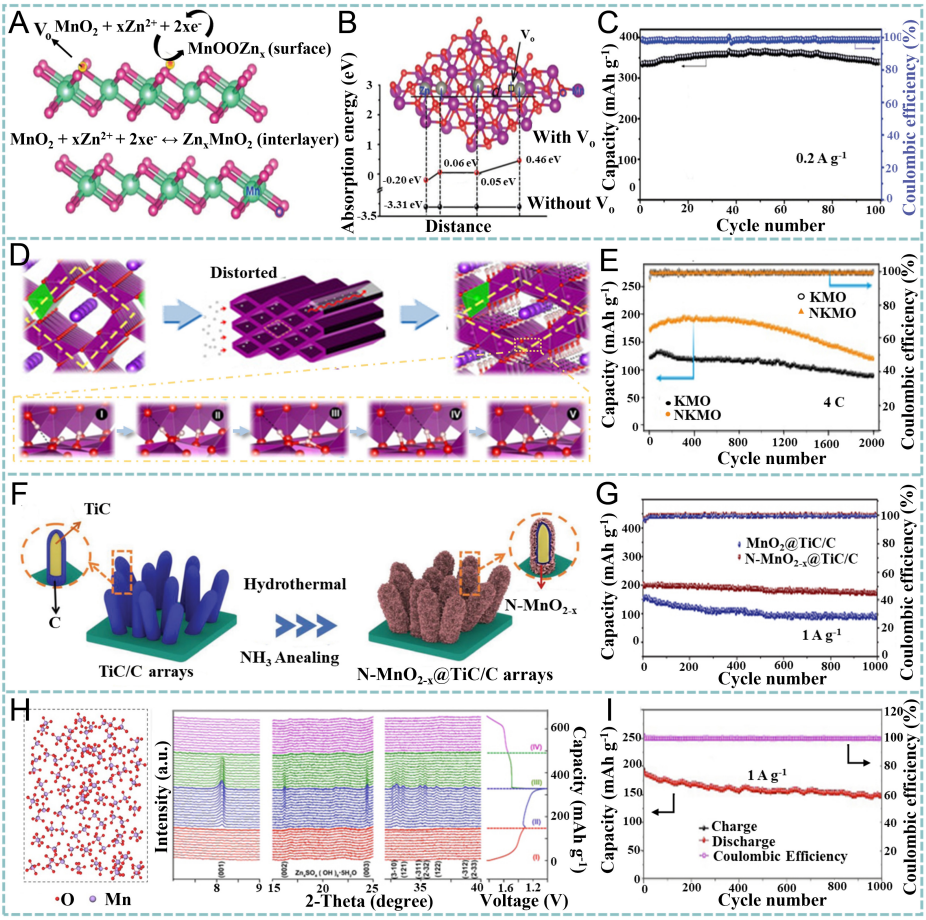

Figure 10. (A) Zn^{2+} storage mechanism for V_O-MnO_2. (B) comparison of adsorption energies for Zn^{2+} on δ-MnO_2 and V_O-MnO_2. (C) cycling performance of V_O-MnO_2 at 0.2 A g^{-1}. Reproduced with permission[136]. Copyright 2019, Wiley-VCH. (D) Zn^{2+} storage in Ni-doped MnO_2 regulated by TO distortion. (E) cycling performance of Ni-doped MnO_2 at 4 C. Reproduced with permission[138]. Copyright 2021, Wiley-VCH. (F) fabrication of N-MnO_{2-x}@TiC/C arrays. (G) cycling capability of MnO_{2-x}@TiC/C and N-MnO_{2-x}@TiC/C at 1.0 A g^{-1}. Reproduced with permission[140]. Copyright 2019, Wiley-VCH. (H) structure of A-$MnO_{2-\delta}$ and *in-situ* XRD patterns during second charge/discharge cycle. (I) cycling performance of A-$MnO_{2-\delta}$ at 1 A g^{-1}. Reproduced with permission[141]. Copyright 2020, Elsevier. KMO: $K_{0.8}Mn_8O_{16}$; NKMO: $Ni_{0.052}K_{0.119}Mn_{0.948}O_2-0.208H_2O$.

(~235 mAh g^{-1}). As shown in Figure 10E, the long-term cycling stability of the Zn/KMO and Zn/NKMO cells examined at 4 C indicated that NKMO showed a slight sacrifice in capacity (73.6% for KMO *vs.* 71.4% for NKMO after 2000 cycles).

Alternatively, Wang *et al.* reported a Ce-doped MnO_2 nanorod-like electrode material synthesized by a hydrothermal method[139]. Cerium doping induced a structural transformation of MnO_2 from its original β-phase to the α-phase, along with the appearance of a [2 × 2] tunnel structure. Its electrochemical properties were investigated using zinc as an anode, 2 M $ZnSO_4$ and 0.1 M $MnSO_4$ as an electrolyte, glass fiber as a separator and the prepared materials as the cathode. Compared to β-MnO_2, 0.1 mmol Ce doping displayed a higher initial capacity and Coulombic efficiency of 134 mAh g^{-1} at 5 C and 82%. More importantly, after 100 cycles, the capacity retention of 0.1 mmol Ce doping was almost twice as high as that of β-MnO_2 at such a high current density. When the rate was in the range of 1-5 C, the 0.1 mmol Ce-doped electrode had high discharge capacities, indicating a better rate capability (308 mAh g^{-1}). Additionally, the galvanostatic intermittent titration technique (GITT) was used to calculate the chemical diffusion

coefficient of Zn^{2+} in the two electrode materials. The diffusion coefficient of Zn^{2+} was improved by one to two orders of magnitude for the 0.1 mmol Ce-doped cathode than the β-MnO_2 cathode. Moreover, Zhang *et al.* simultaneously introduced oxygen vacancies and heteroatom doping into MnO_2 to form a Ndoped MnO_{2-x} ($NMnO_{2-x}$) branch on the surface TiC/C nanorod array ($NMnO_{2-x}$@TiC/C) for ZIBs [Figure 10F][140]. DFT calculations indicated that the combination of oxygen vacancies and N doping greatly improved the conductivity of MnO_2 with a much narrower bandgap (0.1 eV). The electrochemical performance of N-MnO_{2-x}@TiC/C was studied in an aqueous solution of 2 M $ZnSO_4$ and 0.2 M $MnSO_4$. The designed $NMnO_{2-x}$@TiC/C electrode showed improved Zn^{2+} storage performance with faster reaction kinetics, higher capacity (285 mAh g^{-1} at 0.2 A g^{-1}) and excellent cycling performance. After 1000 cycles at 1 A g^{-1}, the N-MnO_{2-x}@TiC/C electrode delivered a reversible capacity of 172.7 mAh g^{-1} with a capacity retention of 84.7% [Figure 10G], higher than its MnO_2@TiC/C counterpart with a reversible capacity of 84.8 mAh g^{-1} (capacity retention of 55.6%).

Amorphous structures with disordered atomic arrangements and abundant structural defects that may lead to enhanced ion diffusion kinetics, improved capacity and alleviated volume expansion are considered to be promising cathode candidates for ZIBs[55,90]. Cai *et al.* demonstrated the feasibility of amorphous MnO_2 (A-$MnO_{2-\delta}$, δ was estimated to be 0.12) in ZIBs and studied the structural evolution of A-$MnO_{2-\delta}$ in 2 M $ZnSO_4$ and 0.2 M $MnSO_4$[141]. *In-situ* XRD profiles were collected at different states in the second discharge/charge cycle [Figure 10H]. Accordingly, the Zn^{2+} storage in A-$MnO_{2-\delta}$ can be divided into four stages: (I: 1.85-1.30 V) no observable peak was found, suggesting that the cation insertion in the A-$MnO_{2-\delta}$ did not change the amorphous structure or generate a new crystalline structure; (II: 1.3-1.0 V) layered $Zn_4SO_4(OH)_6{\cdot}5H_2O$ was generated, as evidenced by a new set of diffraction peaks at 8.1°, 16.2°, 24.4°, 32.7°, 33.5°, 34.9°, 35.3°, 36.3° and 38.6° (JCPDS No. 39-0688); (III: 1.0-1.5 V) the peaks of $Zn_4SO_4(OH)_6{\cdot}5H_2O$ became weakened gradually and completely disappeared at a capacity of 157.3 mAh g^{-1}; (IV: 1.50-1.85 V) no other peaks appeared, suggesting ion extraction from the amorphous Mn-based compound. The A-$MnO_{2-\delta}$ cathode exhibited a reversible *capacity* of 147 mAh g^{-1} at 1 A g^{-1} with a capacity retention of 78% after 1000 cycles [Figure 10I].

Hybridization

Hybridization has been confirmed as a useful method for improving the performance of MnO_2 in ZIBs[142-146]. Li *et al.* anchored MnO_2 particles on N-doped hollow carbon spheres (NHCSs@MnO_2) *via* a direct reaction between carbon and $KMnO_4$ [Figure 11A][147]. The hollow porous carbon nanospheres provided large interfaces, thus ensuring the fast transport of ions/electrons. The obtained NHCSs@MnO_2 exhibited improved performance for Zn^{2+} storage in 2 M $ZnSO_4$ and 0.1 M $MnSO_4$ with an excellent reversible capacity of ~206 mAh g^{-1} and a retention ratio of 89.5% after 200 cycles at 0.1 A g^{-1} [Figure 11B]. Zhang *et al.* used a CNT network as a conductive scaffold on which conformable MnO_2 sheath and rough poly(3, 4-ethylenedioxythiophene) (PEDOT) protective layers were deposited sequentially to form a binder-free CNT/MnO_2/PEDOT (CMOP) electrode[Figure 11C][148]. CNT/MnO_2 (CMO) was also prepared as a control sample. The PEDOT layers prevented MnO_2 from dissolution, which effectively boosted the cycling life of the battery. The electrochemical behavior of MnO_2, MnO_2/PEDOT, CMO and CMOP was evaluated in 2 M $ZnCl_2$ and 0.4 M $MnSO_4$. As demonstrated, the CMOP cathode delivered a maximum specific capacity of 306.1 mAh g^{-1} at 1.1 A g^{-1} and 176.8 mAh g^{-1} at 10.8 A g^{-1} and good long-term stability with a capacity retention of 81.3% after 2000 charge/discharge cycles [Figure 11D].

Alternatively, Zhu *et al.* hybridized MnO_2 nanosheets with a V_2CT_x MXene (K-V_2C@MnO_2) by K^+ intercalation, followed by a hydrothermal growth strategy [Figure 11E][149]. It was found that the adsorbed K^+ on the V_2C surface facilitated the growth of K-birnessite MnO_2, hydrogen bonds existed between

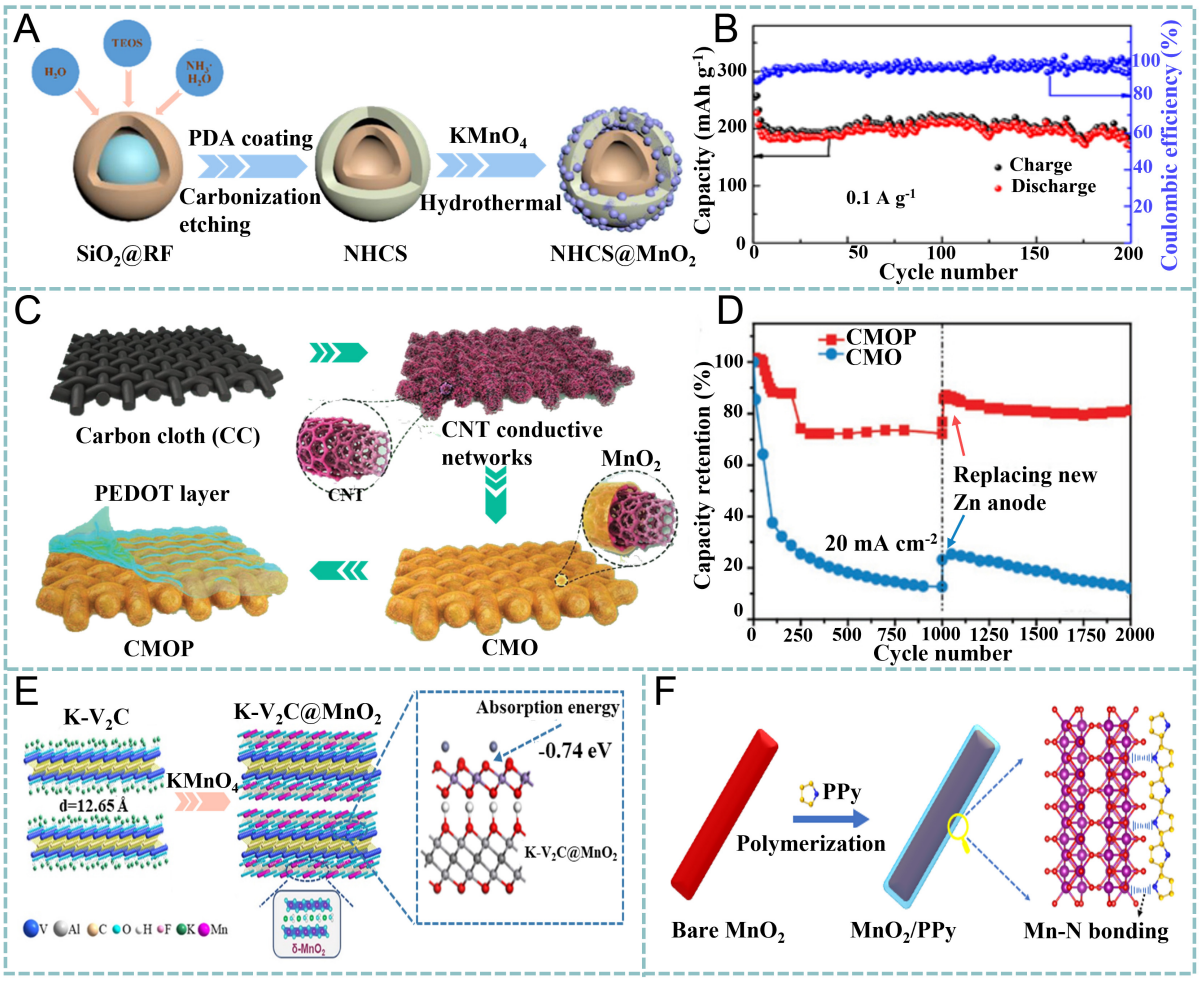

Figure 11. (A) Synthesis of SiO_2@phenol-formaldehyde resin (RF), SiO_2@RF@polydopamine (PDA), NHCSs and NHCSs@MnO_2 composites using tetraethoxysilane (TEOS) as Si source. (B) cyclic performance of NHCSs@MnO_2 at 100 mA g^{-1} for 200 cycles. Reproduced with permission[147]. Copyright 2020, Elsevier. (C) 3D structure of CNT conductive networks and fabrication of CMOP cathodes. (D) long-term cycling performance of CMO and CMOP electrodes. Reproduced with permission[148]. Copyright 2019, Wiley-VCH. (E) synthesis and structural analysis of K-V_2C@MnO_2 and calculated absorption energies for Zn^{2+} on the surfaces of perfect MnO_2-V_2C and δ-MnO_2. Reproduced with permission[149]. Copyright 2021, American Chemical Society. (F) preparation of MnO_2/PPy nanorod. Reproduced with permission[150]. Copyright 2020, Elsevier. CNT: carbon nanotube; CMO: CNT/MnO_2; CMOP: CNT/MnO2/PEDOT; NHCS: N-doped hollow carbon sphere; PEDOT: poly(3,4-ethylenedioxythiophene).

MnO_2 (O) and K-V_2C (H from functional groups), and the Gibbs free energy of Zn^{2+} adsorption in V_2C@MnO_2 was lowered in comparison with pristine δ-MnO_2. The performance of K-V_2C@MnO_2 was evaluated in 2.0 M $ZnSO_4$ and 0.25 M $MnSO_4$. A remarkable capacity of 408.1 mAh g^{-1} at 0.3 A g^{-1} was achieved and 119.2 mAh g^{-1} was retained after 10,000 cycles at 10 A g^{-1}. Huang *et al.* attempted to coat a thin layer of polypyrrole (PPy) to slow the interfacial electrochemical kinetics and prevent the dissolution of MnO_2 [Figure 11F][150]. Interestingly, strong Mn-N bonds were found at the interface of MnO_2 and PPy. DFT calculations revealed that the energy barrier for Mn escape was increased to 6.76 eV owing to the Mn-N bond. The performance of MnO_2 and MnO_2/PPy was tested in 2 M $ZnSO_4$ and 0.1 M $MnSO_4$. In comparison with MnO_2 (133 mAh g^{-1}), MnO_2/PPy provided 256 mAh g^{-1} after 50 cycles at 100 mA g^{-1} without capacity fade.

SUMMARY AND OUTLOOK

Summary

This review focuses on the applications of MnO_2 for aqueous energy storage (SCs and ZIBs) and summarizes and compares the similarities and differences of the corresponding charge storage mechanisms and the principles for materials modification [Table 1].

Charge storage mechanisms

In the case of SCs, the surface redox reactions and bulk intercalation of electrolyte ions are the two dominating mechanisms for charge storage in MnO_2 Equations (10) and (11). The pH of the electrolyte severely affects the electrochemical reactions during charge/discharge. In an acidic solution, an irreversible reaction occurs between H^+ and MnOOH, forming dissoluble Mn^{2+}. In an alkaline solution, a passivation layer of $Mn(OH)_2$ is generated as a result of the reaction between MnO_2 and OH^-. In a neutral electrolyte, the disproportionation of Mn^{3+} to dissoluble Mn^{2+} is usually observed. Considering the chemical stability of the zinc metal anode, a near-neutral electrolyte is usually selected (e.g., $ZnSO_4$ aqueous solution) for ZIBs. Three possible mechanisms are proposed: (i) intercalation/deintercalation of Zn^{2+}; (ii) co-insertion/extraction of H^+/Zn^{2+}; and (iii) dissolution-deposition of MnO_2/Mn^{2+}. Although it is still under debate, the charge storage mechanism generally involves the insertion of H^+ (fast kinetics) to generate MnOOH, the insertion of Zn^{2+} (slow kinetics) to generate Zn_2MnO_4 and the irreversible deposition of ZSH on the surface of electrodes. Indeed, the existing works on designing MnO_2 cathodes for ZIBs are very similar to the explorations of MnO_2-based SCs using near-neutral electrolytes (zinc salt-based aqueous electrolyte, e.g., $ZnSO_4$, $ZnCl_2$, ZnTFSI or $Zn(CF_3SO_3)_2$). However, different from the monovalent cations mostly investigated in SCs, Zn^{2+} has a larger hydrated ionic radius, higher desolvation energy barrier and stronger electrostatic interaction with MnO_2, all of which induce complex electrode reactions and structural instability in MnO_2 cathodes for ZIBs.

MnO_2 modification methods

Low electrical conductivity, structural instability and slow electrode reaction kinetics are common issues of MnO_2 as electrodes for energy storage. Based on our summary, similar strategies have been adopted for MnO_2 modification in both SCs and ZIBs, including foreign ion/molecular pre-insertion, defect engineering, nanostructural design and hybridization. Typically, the pre-inserted ions/molecules in MnO_2 facilitate the ion intercalation/deintercalation by expanding the interlayer spaces, shield the strong electrostatic interaction between intercalated ions and MnO_2 and stabilize the crystal structure of MnO_2 during ion intercalation/deintercalation. The introduction of oxygen vacancies and heteroatom doping (defect engineering) are effective methods to regulate the electron structure of MnO_2, which significantly affect the electron transport during the redox reaction. Rational nanostructural design contributes to the accessibility of electrolyte ions to active sites, thereby improving the capacity of the electrode. Hybridizing with high conductive carbonaceous materials (e.g., CNTs and rGO) can efficiently improve the conductivity of bare MnO_2, thus boosting the kinetics of the electrode reaction.

Outlook

Although significant efforts have been devoted to the investigation of MnO_2 for potential applications in SCs and ZIBs and there are several prospective aspects that need to be considered:

(1) MnO_2 is considered as one of the most promising candidates for SCs because of its low cost, earth abundance, high theoretical capacitance and environmental benignness. Nevertheless, the performance of MnO_2 in SCs is far from satisfactory. An in-depth understanding of the underlying mechanisms and efficient strategies for performance improvements are highly required.

Table 1. Similarities and differences in using MnO_2 as electrode material in SCs and ZIBs

Classification	Mechanisms	Modification strategies
SCs	☆ Surface redox reaction ☆ Bulk intercalation (no phase transition)	• Nanostructural design • Foreign ion/molecular pre-insertion • Defect engineering • Hybridization
ZIBs	☆ Insertion/extraction of Zn^{2+} ☆ Co-insertion of H^+ and Zn^{2+} ☆ Dissolution-deposition (with phase transition)	• Foreign ion/molecular pre-insertion • Defect engineering • Hybridization

(2) To date, the mechanism for Zn^{2+} storage is still under debate and severely depends on the testing conditions. More efforts are required by employing advanced characterization techniques.

(3) The introduction of oxygen vacancies and heteroatoms is deemed to be an effective method to regulate the properties of MnO_2 for enhancing the charge storage in both SCs and ZIBs. However, since MnO_2 crystals are composed of MnO_6 octahedral units, it remains necessary to quantitatively identify the concentration and position of oxygen vacancies and heteroatoms that play a critical role in governing MnO_2 performance.

(4) The pre-intercalation of cations, water molecules and polymers has been demonstrated to be an effective strategy to enhance the capacitance/capacity and stability of MnO_2. The mechanisms for performance enhancement need to be further investigated.

(5) Hybridization with conductive materials (e.g., graphene and MXenes) is considered a feasible method to efficiently improve the electron transfer/transport of MnO_2. In addition, the interfacial properties between two materials are believed to contribute the performance enhancement. However, a detailed explanation of interface-dependent electrochemical behavior is still required.

(6) Finally, more attention should be paid to the performance decay mechanisms of MnO_2 in SCs and ZIBs, which are the guidelines for future materials design.

DECLARATIONS

Authors' contributions

Preparing the manuscript draft: Dai H, Zhou R
Writing-review: Zhang Z
Editing: Zhou J
Funding acquisition, supervision: Sun G

Availability of data and materials

Not applicable.

Financial support and sponsorship

This work was supported by the National Natural Science Foundation of China (No. 21975123), Anhui Provincial Key R&D Program (No. 2022i01020021) and Six Talent Peaks Project in Jiangsu Province (No. XCL-024).

Conflicts of interest
All authors declared that there are no conflicts of interest.

Ethical approval and consent to participate
Not applicable.

Consent for publication
Not applicable.

Copyright
© The Author(s) 2022.

REFERENCES

1. Gerard O, Numan A, Krishnan S, Khalid M, Subramaniam R, Kasi R. A review on the recent advances in binder-free electrodes for electrochemical energy storage application. *J Energy Storage* 2022;50:104283. DOI
2. Yu C, Gong Y, Chen R, et al. A solid-state fibriform supercapacitor boosted by host-guest hybridization between the carbon nanotube scaffold and MXene nanosheets. *Small* 2018:e1801203. DOI PubMed
3. Xiao J, Han J, Zhang C, Ling G, Kang F, Yang Q. Dimensionality, function and performance of carbon materials in energy storage devices. *Adv Energy Mater* 2022;12:2100775. DOI
4. Liu Y, Xu J, Li J, et al. Pre-intercalation chemistry of electrode materials in aqueous energy storage systems. *Coord Chem Rev* 2022;460:214477. DOI
5. Shin J, Lee J, Park Y, Choi JW. Aqueous zinc ion batteries: focus on zinc metal anodes. *Chem Sci* 2020;11:2028-44. DOI PubMed PMC
6. Dai H, Zhou J, Qin G, Sun G. Enhanced Jahn-Teller distortion boosts molybdenum trioxide's superior lithium ion storage capability. *Dalton Trans* 2022;51:524-31. DOI PubMed
7. Dai H, Wang L, Zhao Y, et al. Recent advances in molybdenum-based materials for lithium-sulfur batteries. *Research* 2021;2021:5130420. DOI PubMed PMC
8. Zhang X, Li Z, Luo L, Fan Y, Du Z. A review on thermal management of lithium-ion batteries for electric vehicles. *Energy* 2022;238:121652. DOI
9. Rivera-barrera J, Muñoz-galeano N, Sarmiento-maldonado H. SoC estimation for lithium-ion batteries: review and future challenges. *Electronics* 2017;6:102. DOI
10. Muralidharan N, Self EC, Dixit M, et al. Next-generation cobalt-free cathodes - a prospective solution to the battery industry's cobalt problem. *Adv Energy Mater* 2022;12:2103050. DOI
11. Li J, Fleetwood J, Hawley WB, Kays W. From materials to cell: state-of-the-art and prospective technologies for lithium-ion battery electrode processing. *Chem Rev* 2022;122:903-56. DOI PubMed
12. Chao D, Zhou W, Xie F, et al. Roadmap for advanced aqueous batteries: from design of materials to applications. *Sci Adv* 2020;6:eaba4098. DOI PubMed PMC
13. Sui Y, Ji X. Anticatalytic strategies to suppress water electrolysis in aqueous batteries. *Chem Rev* 2021;121:6654-95. DOI PubMed
14. Bin D, Wen Y, Wang Y, Xia Y. The development in aqueous lithium-ion batteries. *J Energy Chem* 2018;27:1521-35. DOI
15. Jiang X, Chen Y, Meng X, et al. The impact of electrode with carbon materials on safety performance of lithium-ion batteries: a review. *Carbon* 2022;191:448-70. DOI
16. Liu K, Liu Y, Lin D, Pei A, Cui Y. Materials for lithium-ion battery safety. *Sci Adv* 2018;4:eaas9820. DOI PubMed PMC
17. Su X, Wu Q, Li J, et al. Silicon-based nanomaterials for lithium-ion batteries: a review. *Adv Energy Mater* 2014;4:1300882. DOI
18. Xie J, Lu YC. A retrospective on lithium-ion batteries. *Nat Commun* 2020;11:2499. DOI PubMed PMC
19. Yang Z, Zhang J, Kintner-Meyer MC, et al. Electrochemical energy storage for green grid. *Chem Rev* 2011;111:3577-613. DOI PubMed
20. Yong B, Ma D, Wang Y, Mi H, He C, Zhang P. Understanding the design principles of advanced aqueous zinc-ion battery cathodes: from transport kinetics to structural engineering, and future perspectives. *Adv Energy Mater* 2020;10:2002354. DOI
21. Peng J, Zhang W, Wang S, et al. The emerging electrochemical activation tactic for aqueous energy storage: fundamentals, applications, and future. *Adv Funct Mater* 2022;32:2111720. DOI
22. Lee B, Lee HR, Kim H, Chung KY, Cho BW, Oh SH. Elucidating the intercalation mechanism of zinc ions into α-MnO_2 for rechargeable zinc batteries. *Chem Commun* 2015;51:9265-8. DOI PubMed
23. Tang Y, Zheng S, Xu Y, Xiao X, Xue H, Pang H. Advanced batteries based on manganese dioxide and its composites. *Energy Stor Mater* 2018;12:284-309. DOI
24. Qian J, Jin H, Chen B, et al. Aqueous manganese dioxide ink for paper-based capacitive energy storage devices. *Angew Chem Int Ed Engl* 2015;54:6800-3. DOI PubMed

25. Pan H, Shao Y, Yan P, et al. Reversible aqueous zinc/manganese oxide energy storage from conversion reactions. *Nat Energy* 2016:1. DOI
26. Tang B, Shan L, Liang S, Zhou J. Issues and opportunities facing aqueous Zinc-ion batteries. *Energy Environ Sci* 2019;12:3288-304. DOI
27. Ming J, Guo J, Xia C, Wang W, Alshareef HN. Zinc-ion batteries: materials, mechanisms, and applications. *Mater Sci Eng R Rep* 2019;135:58-84. DOI
28. Fang G, Zhou J, Pan A, Liang S. Recent advances in aqueous Zinc-ion batteries. *ACS Energy Lett* 2018;3:2480-501. DOI
29. Dong C, Xu F, Chen L, Chen Z, Cao Y. Design strategies for high-voltage aqueous batteries. *Small Struct* 2021;2:2100001. DOI
30. Wang F, Wu X, Yuan X, et al. Latest advances in supercapacitors: from new electrode materials to novel device designs. *Chem Soc Rev* 2017;46:6816-54. DOI PubMed
31. Augustyn V, Simon P, Dunn B. Pseudocapacitive oxide materials for high-rate electrochemical energy storage. *Energy Environ Sci* 2014;7:1597. DOI
32. Huang J, Yuan K, Chen Y. Wide voltage aqueous asymmetric supercapacitors: advances, strategies, and challenges. *Adv Funct Mater* 2022;32:2108107. DOI
33. Wang S, Li T, Yin Y, Chang N, Zhang H, Li X. High-energy-density aqueous zinc-based hybrid supercapacitor-battery with uniform zinc deposition achieved by multifunctional decoupled additive. *Nano Energy* 2022;96:107120. DOI
34. Li H, Ma L, Han C, et al. Advanced rechargeable zinc-based batteries: recent progress and future perspectives. *Nano Energy* 2019;62:550-87. DOI
35. Zhang K, Han X, Hu Z, Zhang X, Tao Z, Chen J. Nanostructured Mn-based oxides for electrochemical energy storage and conversion. *Chem Soc Rev* 2015;44:699-728. DOI PubMed
36. Zhong C, Deng Y, Hu W, Qiao J, Zhang L, Zhang J. A review of electrolyte materials and compositions for electrochemical supercapacitors. *Chem Soc Rev* 2015;44:7484-539. DOI PubMed
37. He P, Chen Q, Yan M, et al. Building better Zinc-ion batteries: a materials perspective. *EnergyChem* 2019;1:100022. DOI
38. Lv Y, Xiao Y, Ma L, Zhi C, Chen S. Recent advances in electrolytes for "beyond aqueous" Zinc-ion batteries. *Adv Mater* 2022;34:e2106409. DOI PubMed
39. Zhou T, Zhu L, Xie L, et al. Cathode materials for aqueous Zinc-ion batteries: a mini review. *J Colloid Interface Sci* 2022;605:828-50. DOI
40. Gao Y, Zhao L. Review on recent advances in nanostructured transition-metal-sulfide-based electrode materials for cathode materials of asymmetric supercapacitors. *Chem Eng J* 2022;430:132745. DOI
41. Kumar S, Saeed G, Zhu L, Hui KN, Kim NH, Lee JH. 0D to 3D carbon-based networks combined with pseudocapacitive electrode material for high energy density supercapacitor: a review. *Chem Eng J* 2021;403:126352. DOI
42. Hu Y, Wu Y, Wang J. Manganese-oxide-based electrode materials for energy storage applications: how close are we to the theoretical capacitance? *Adv Mater* 2018;30:e1802569. DOI PubMed
43. Kumar A, Sanger A, Kumar A, Mishra YK, Chandra R. Performance of high energy density symmetric supercapacitor based on sputtered MnO_2 nanorods. *ChemistrySelect* 2016;1:3885-91. DOI
44. Yu N, Yin H, Zhang W, Liu Y, Tang Z, Zhu M. High-performance fiber-shaped all-solid-state asymmetric supercapacitors based on ultrathin MnO_2 nanosheet/carbon fiber cathodes for wearable electronics. *Adv Energy Mater* 2016;6:1501458. DOI
45. Radhamani AV, Shareef KM, Rao MS. ZnO@MnO_2 core-shell nanofiber cathodes for high performance asymmetric supercapacitors. *ACS Appl Mater Interfaces* 2016;8:30531-42. DOI PubMed
46. Zhou D, Lin H, Zhang F, et al. Freestanding MnO_2 nanoflakes/porous carbon nanofibers for high-performance flexible supercapacitor electrodes. *Electrochim Acta* 2015;161:427-35. DOI
47. Cai K, Luo SH, Feng J, et al. Recent advances on spinel zinc manganate cathode materials for Zinc-ion batteries. *Chem Rec* 2022;22:e202100169. DOI PubMed
48. Davoglio RA, Cabello G, Marco JF, Biaggio SR. Synthesis and characterization of α-MnO_2 nanoneedles for electrochemical supercapacitors. *Electrochim Acta* 2018;261:428-35. DOI
49. Guo C, Liu H, Li J, et al. Ultrathin δ-MnO_2 nanosheets as cathode for aqueous rechargeable zinc ion battery. *Electrochim Acta* 2019;304:370-7. DOI
50. Li Y, Zhang D, Huang S, Yang HY. Guest-species-incorporation in manganese/vanadium-based oxides: towards high performance aqueous Zinc-ion batteries. *Nano Energy* 2021;85:105969. DOI
51. Zhang Z, Li W, Shen Y, et al. Issues and opportunities of manganese-based materials for enhanced Zn-ion storage performances. *J Energy Storage* 2022;45:103729. DOI
52. Xie Q, Cheng G, Xue T, et al. Alkali ions pre-intercalation of δ-MnO_2 nanosheets for high-capacity and stable Zn-ion battery. *Mater Today Energy* 2022;24:100934. DOI
53. Wang M, Zheng X, Zhang X, et al. Opportunities of aqueous manganese-based batteries with deposition and stripping chemistry. *Adv Energy Mater* 2021;11:2002904. DOI
54. Nam KW, Kim H, Choi JH, Choi JW. Crystal water for high performance layered manganese oxide cathodes in aqueous rechargeable zinc batteries. *Energy Environ Sci* 2019;12:1999-2009. DOI
55. Wu Y, Fee J, Tobin Z, et al. Amorphous manganese oxides: an approach for reversible aqueous Zinc-ion batteries. *ACS Appl Energy Mater* 2020;3:1627-33. DOI

56. Li S, Liu Q, Qi L, Lu L, Wang H. Progress in research on manganese dioxide electrode materials for electrochemical capacitors. *Chinese J Anal Chem* 2012;40:339-46. DOI
57. Wang J, Dong S, Ding B, et al. Pseudocapacitive materials for electrochemical capacitors: from rational synthesis to capacitance optimization. *Natl Sci Rev* 2017;4:71-90. DOI
58. Brousse T, Toupin M, Dugas R, Athouël L, Crosnier O, Bélanger D. Crystalline MnO_2 as possible alternatives to amorphous compounds in electrochemical supercapacitors. *J Electrochem Soc* 2006;153:A2171. DOI
59. Yan J, Fan Z, Wei T, Qian W, Zhang M, Wei F. Fast and reversible surface redox reaction of graphene-MnO_2 composites as supercapacitor electrodes. *Carbon* 2010;48:3825-33. DOI
60. Zhang Y, An Y, Jiang J, et al. High performance aqueous sodium-ion capacitors enabled by pseudocapacitance of layered MnO_2. *Energy Technol* 2018;6:2146-53. DOI
61. Chen Q, Jin J, Kou Z, et al. Zn^{2+} pre-intercalation stabilizes the tunnel structure of MnO_2 nanowires and enables Zinc-ion hybrid supercapacitor of battery-level energy density. *Small* 2020;16:e2000091. DOI
62. Tang X, Zhu S, Ning J, Yang X, Hu M, Shao J. Charge storage mechanisms of manganese dioxide-based supercapacitors: a review. *New Carbon Mater* 2021;36:702-10. DOI
63. Guo W, Yu C, Li S, et al. Strategies and insights towards the intrinsic capacitive properties of MnO_2 for supercapacitors: challenges and perspectives. *Nano Energy* 2019;57:459-72. DOI
64. Kim SJ, Wu D, Sadique N, et al. Unraveling the dissolution-mediated reaction mechanism of α-MnO_2 cathodes for aqueous Zn-ion batteries. *Small* 2020;16:e2005406. DOI PubMed
65. Qiu C, Zhu X, Xue L, et al. The function of Mn^{2+} additive in aqueous electrolyte for Zn/δ-MnO_2 battery. *Electrochim Acta* 2020;351:136445. DOI
66. Julien CM, Mauger A. Nanostructured MnO_2 as electrode materials for energy storage. *Nanomaterials* 2017;7:396. DOI PubMed PMC
67. Majumdar D. Review on current progress of MnO_2-based ternary nanocomposites for supercapacitor applications. *ChemElectroChem* 2021;8:291-336. DOI
68. Shin J, Seo JK, Yaylian R, Huang A, Meng YS. A review on mechanistic understanding of MnO_2 in aqueous electrolyte for electrical energy storage systems. *Int Mater Rev* 2020;65:356-87. DOI
69. Messaoudi B, Joiret S, Keddam M, Takenouti H. Anodic behaviour of manganese in alkaline medium. *Electrochim Acta* 2001;46:2487-98. DOI
70. Roberts AJ, Slade RC. Effect of specific surface area on capacitance in asymmetric carbon/α-MnO_2 supercapacitors. *Electrochim Acta* 2010;55:7460-9. DOI
71. Wu B, Zhang G, Yan M, et al. Graphene scroll-coated α-MnO_2 nanowires as high-performance cathode materials for aqueous Zn-ion battery. *Small* 2018;14:e1703850. DOI PubMed
72. Wang J, Dong L, Xu C, Ren D, Ma X, Kang F. Polymorphous supercapacitors constructed from flexible three-dimensional carbon network/Polyaniline/MnO_2 composite textiles. *ACS Appl Mater Interfaces* 2018;10:10851-9. DOI PubMed
73. Fu Y, Gao X, Zha D, Zhu J, Ouyang X, Wang X. Yolk-shell-structured MnO_2 microspheres with oxygen vacancies for high-performance supercapacitors. *J Mater Chem A* 2018;6:1601-11. DOI
74. Fu W, Zhao E, Ren X, Magasinski A, Yushin G. Hierarchical fabric decorated with carbon nanowire/metal oxide nanocomposites for 1.6 V wearable aqueous supercapacitors. *Adv Energy Mater* 2018;8:1703454. DOI
75. Qi H, Bo Z, Yang S, et al. Hierarchical nanocarbon-MnO_2 electrodes for enhanced electrochemical capacitor performance. *Energy Stor Mater* 2019;16:607-18. DOI
76. Chen L, Zhang M, Yang X, et al. Sandwich-structured MnO_2@N-doped carbon@MnO_2 nanotubes for high-performance supercapacitors. *J Alloys Compd* 2017;695:3339-47. DOI
77. Han D, Jing X, Xu P, Ding Y, Liu J. Facile synthesis of hierarchical hollow ε-MnO_2 spheres and their application in supercapacitor electrodes. *J Solid State Chem* 2014;218:178-83. DOI
78. Xiong P, Ma R, Sakai N, Bai X, Li S, Sasaki T. Redox active cation intercalation/deintercalation in two-dimensional layered MnO_2 nanostructures for high-rate electrochemical energy storage. *ACS Appl Mater Interfaces* 2017;9:6282-91. DOI PubMed
79. Jabeen N, Xia Q, Savilov SV, Aldoshin SM, Yu Y, Xia H. Enhanced pseudocapacitive performance of α-MnO_2 by cation preinsertion. *ACS Appl Mater Interfaces* 2016;8:33732-40. DOI PubMed
80. Gao P, Metz P, Hey T, et al. The critical role of point defects in improving the specific capacitance of δ-MnO_2 nanosheets. *Nat Commun* 2017;8:14559. DOI PubMed PMC
81. Chen S, Zhang M, Ma X, Li L, Zhou X, Zhang Z. Asymmetric supercapacitors by integrating high content Na^+/K^+-inserted MnO_2 nanosheets and layered $Ti_3C_2T_x$ paper. *Electrochim Acta* 2020;332:135497. DOI
82. Zhao Q, Song A, Ding S, et al. Preintercalation strategy in manganese oxides for electrochemical energy storage: review and prospects. *Adv Mater* 2020;32:e2002450. DOI PubMed
83. Peng H, Fan H, Sui J, Wang C, Zhang W, Wang W. Sodium in situ intercalated ultrathin δ-MnO_2 flakes electrode with enhanced intercalation capacitive performance for asymmetric supercapacitors. *ChemistrySelect* 2020;5:869-74. DOI
84. Jabeen N, Hussain A, Xia Q, Sun S, Zhu J, Xia H. High-performance 2.6 V aqueous asymmetric supercapacitors based on in situ formed $Na_{0.5}MnO_2$ nanosheet assembled nanowall arrays. *Adv Mater* 2017;29:1700804. DOI
85. Jiang H, Wang Z, Yang Q, et al. A novel $MnO_2/Ti_3C_2T_x$ MXene nanocomposite as high performance electrode materials for flexible

supercapacitors. *Electrochim Acta* 2018;290:695-703. DOI
86. Chi HZ, Li Y, Xin Y, Qin H. Boron-doped manganese dioxide for supercapacitors. *Chem Commun* 2014;50:13349-52. DOI PubMed
87. Choi C, Sim HJ, Spinks GM, Lepró X, Baughman RH, Kim SJ. Elastomeric and dynamic MnO_2/CNT core-shell structure coiled yarn supercapacitor. *Adv Energy Mater* 2016;6:1502119. DOI
88. Wang Y, Zhang Y, Gao Y, Sheng G, ten Elshof JE. Defect engineering of MnO_2 nanosheets by substitutional doping for printable solid-state micro-supercapacitors. *Nano Energy* 2020;68:104306. DOI
89. Wang J, Wang J, Liu H, et al. A highly flexible and lightweight MnO_2/graphene membrane for superior Zinc-ion batteries. *Adv Funct Mater* 2021;31:2007397. DOI
90. Tong H, Li T, Liu J, et al. Fabrication of the oxygen vacancy amorphous MnO_2/Carbon nanotube as cathode for advanced aqueous Zinc-ion batteries. *Energy Technol* 2021;9:2000769. DOI
91. Shi J, Wang S, Wang Q, et al. A new flexible Zinc-ion capacitor based on δ-MnO_2@Carbon cloth battery-type cathode and MXene@Cotton cloth capacitor-type anode. *J Power Sources* 2020;446:227345. DOI
92. Zhao L, Wang W, Zhao H, et al. Controlling oxygen vacancies through gas-assisted hydrothermal method and improving the capacitive properties of MnO_2 nanowires. *Appl Surf Sci* 2019;491:24-31. DOI
93. Yan L, Shen C, Niu L, et al. Experimental and theoretical investigation of the effect of oxygen vacancies on the electronic structure and pseudocapacitance of MnO_2. *ChemSusChem* 2019;12:3571-81. DOI PubMed
94. Zhai T, Xie S, Yu M, et al. Oxygen vacancies enhancing capacitive properties of MnO_2 nanorods for wearable asymmetric supercapacitors. *Nano Energy* 2014;8:255-63. DOI
95. Ou T, Hsu C, Hu C. Synthesis and characterization of sodium-doped MnO_2 for the aqueous asymmetric supercapacitor application. *J Electrochem Soc* 2015;162:A5124-32. DOI
96. Li J, Ren Y, Wang S, Ren Z, Yu J. Transition metal doped MnO_2 nanosheets grown on internal surface of macroporous carbon for supercapacitors and oxygen reduction reaction electrocatalysts. *Appl Mater Today* 2016;3:63-72. DOI
97. Kang J, Hirata A, Kang L, et al. Enhanced supercapacitor performance of MnO_2 by atomic doping. *Angew Chem Int Ed Engl* 2013;52:1664-7. DOI PubMed
98. Wang Z, Wang F, Li Y, Hu J, Lu Y, Xu M. Interlinked multiphase Fe-doped MnO_2 nanostructures: a novel design for enhanced pseudocapacitive performance. *Nanoscale* 2016;8:7309-17. DOI PubMed
99. Peng R, Wang H, Wei X, Wu Z, Yu P, Luo Y. One-step synthesis of vacancy-rich MnO_{2-x}/reduced graphene oxide composite film for high electrochemical performance. *ChemElectroChem* 2019;6:1122-8. DOI
100. Shi P, Li L, Hua L, et al. Design of amorphous manganese oxide@multiwalled carbon nanotube fiber for robust solid-state supercapacitor. *ACS Nano* 2017;11:444-52. DOI
101. Gou L, Xue D, Mou K, et al. α-MnO_2@In_2O_3 nanotubes as cathode material for aqueous rechargeable Zn-ion battery with high electrochemical performance. *J Electrochem Soc* 2019;166:A3362-8. DOI
102. Zhang J, Li Y, Zhang Y, et al. The enhanced adhesion between overlong TiN_xO_y/MnO_2 nanoarrays and Ti substrate: towards flexible supercapacitors with high energy density and long service life. *Nano Energy* 2018;43:91-102. DOI
103. Xu J, Sun Y, Lu M, et al. Fabrication of hierarchical $MnMoO_4 \cdot H_2O$@MnO_2 core-shell nanosheet arrays on nickel foam as an advanced electrode for asymmetric supercapacitors. *Chem Eng J* 2018;334:1466-76. DOI
104. Shinde PA, Lokhande VC, Patil AM, Ji T, Lokhande CD. Single-step hydrothermal synthesis of WO_3-MnO_2 composite as an active material for all-solid-state flexible asymmetric supercapacitor. *Int J Hydrog Energy* 2018;43:2869-80. DOI
105. Zhu S, Li L, Liu J, et al. Structural directed growth of ultrathin parallel birnessite on β-MnO_2 for high-performance asymmetric supercapacitors. *ACS Nano* 2018;12:1033-42. DOI PubMed
106. Liu N, Su Y, Wang Z, et al. Electrostatic-interaction-assisted construction of 3D networks of manganese dioxide nanosheets for flexible high-performance solid-state asymmetric supercapacitors. *ACS Nano* 2017;11:7879-88. DOI PubMed
107. Zhou J, Yu J, Shi L, et al. A conductive and highly deformable all-pseudocapacitive composite paper as supercapacitor electrode with improved areal and volumetric capacitance. *Small* 2018;14:e1803786. DOI PubMed
108. Chen Q, Meng Y, Hu C, et al. MnO_2-modified hierarchical graphene fiber electrochemical supercapacitor. *J Power Sources* 2014;247:32-9. DOI
109. Tan X, Liu S, Guo Q, et al. Synthesis and characterisation of amorphous MnO_2/CNT via solid-state microwave for high-performance supercapacitors. *Int J Energy Res* 2020;44:4556-67. DOI
110. Chen Y, Zhang X, Xu C, Xu H. The fabrication of asymmetry supercapacitor based on $MWCNT_s$/MnO_2/PPy composites. *Electrochim Acta* 2019;309:424-31. DOI
111. Zhang QZ, Zhang D, Miao ZC, Zhang XL, Chou SL. Research progress in MnO_2-carbon based supercapacitor electrode materials. *Small* 2018;14:e1702883. DOI PubMed
112. Yu G, Hu L, Vosgueritchian M, et al. Solution-processed graphene/MnO_2 nanostructured textiles for high-performance electrochemical capacitors. *Nano Lett* 2011;11:2905-11. DOI PubMed
113. Jia H, Cai Y, Lin J, et al. Heterostructural graphene quantum dot/MnO_2 nanosheets toward high-potential window electrodes for high-performance supercapacitors. *Adv Sci* 2018;5:1700887. DOI PubMed PMC
114. Song M, Tan H, Chao D, Fan HJ. Recent advances in Zn-ion batteries. *Adv Funct Mater* 2018;28:1802564. DOI
115. Jia X, Liu C, Neale ZG, Yang J, Cao G. Active materials for aqueous Zinc ion batteries: synthesis, crystal structure, morphology, and electrochemistry. *Chem Rev* 2020;120:7795-866. DOI PubMed

116. Alfaruqi MH, Gim J, Kim S, et al. Enhanced reversible divalent zinc storage in a structurally stable α-MnO_2 nanorod electrode. *J Power Sources* 2015;288:320-7. DOI
117. Lee B, Yoon CS, Lee HR, Chung KY, Cho BW, Oh SH. Electrochemically-induced reversible transition from the tunneled to layered polymorphs of manganese dioxide. *Sci Rep* 2014;4:6066. DOI PubMed PMC
118. Alfaruqi MH, Mathew V, Gim J, et al. Electrochemically induced structural transformation in a γ-MnO_2 cathode of a high capacity Zinc-ion battery system. *Chem Mater* 2015;27:3609-20. DOI
119. Deng Y, Wan L, Xie Y, Qin X, Chen G. Recent advances in Mn-based oxides as anode materials for lithium ion batteries. *RSC Adv* 2014;4:23914-35. DOI
120. Li F, Liu Y, Wang G, et al. The design of flower-like C-MnO_2 nanosheets on carbon cloth toward high-performance flexible Zinc-ion batteries. *J Mater Chem A* 2021;9:9675-84. DOI
121. Liu G, Huang H, Bi R, Xiao X, Ma T, Zhang L. K^+ pre-intercalated manganese dioxide with enhanced Zn^{2+} diffusion for high rate and durable aqueous Zinc-ion batteries. *J Mater Chem A* 2019;7:20806-12. DOI
122. Liu M, Zhao Q, Liu H, et al. Tuning phase evolution of β-MnO_2 during microwave hydrothermal synthesis for high-performance aqueous Zn ion battery. *Nano Energy* 2019;64:103942. DOI
123. Li G, Huang Z, Chen J, et al. Rechargeable Zn-ion batteries with high power and energy densities: a two-electron reaction pathway in birnessite MnO_2 cathode materials. *J Mater Chem A* 2020;8:1975-85. DOI
124. Jin Y, Zou L, Liu L, et al. Joint charge storage for high-rate aqueous zinc-manganese dioxide batteries. *Adv Mater* 2019;31:e1900567. DOI PubMed
125. Guo X, Zhou J, Bai C, Li X, Fang G, Liang S. Zn/MnO_2 battery chemistry with dissolution-deposition mechanism. *Mater Today Energy* 2020;16:100396. DOI
126. Peng H, Fan H, Yang C, Tian Y, Wang C, Sui J. Ultrathin δ-MnO_2 nanoflakes with Na^+ intercalation as a high-capacity cathode for aqueous Zinc-ion batteries. *RSC Adv* 2020;10:17702-12. DOI
127. Sun T, Nian Q, Zheng S, Shi J, Tao Z. Layered $Ca_{0.28}MnO_2{\cdot}0.5H_2O$ as a high performance cathode for aqueous Zinc-ion battery. *Small* 2020;16:e2000597. DOI
128. Fang G, Zhu C, Chen M, et al. Suppressing manganese dissolution in potassium manganate with rich oxygen defects engaged high-energy-density and durable aqueous Zinc-ion battery. *Adv Funct Mater* 2019;29:1808375. DOI
129. Zhai T, Wan L, Sun S, et al. Phosphate ion functionalized Co_3O_4 ultrathin nanosheets with greatly improved surface reactivity for high performance pseudocapacitors. *Adv Mater* 2017;29:1604167. DOI
130. Zhang Y, Deng S, Pan G, et al. Introducing oxygen defects into phosphate ions intercalated manganese dioxide/vertical multilayer graphene arrays to boost flexible Zinc ion storage. *Small Methods* 2020;4:1900828. DOI
131. Huang J, Wang Z, Hou M, et al. Polyaniline-intercalated manganese dioxide nanolayers as a high-performance cathode material for an aqueous Zinc-ion battery. *Nat Commun* 2018;9:2906. DOI PubMed PMC
132. Zhang Q, Yang Z, Ji H, et al. Issues and rational design of aqueous electrolyte for Zn-ion batteries. *SusMat* 2021;1:432-47. DOI
133. Wang D, Wang L, Liang G, et al. A superior δ-MnO_2 cathode and a self-healing Zn-δ-MnO_2 battery. *ACS Nano* 2019;13:10643-52. DOI
134. Han M, Huang J, Liang S, et al. Oxygen defects in β-MnO_2 enabling high-performance rechargeable aqueous zinc/manganese dioxide battery. *iScience* 2020;23:100797. DOI PubMed PMC
135. Zhao J, Xu Z, Zhou Z, et al. A safe flexible self-powered wristband system by integrating defective MnO_{2-x} nanosheet-based Zinc-ion batteries with perovskite solar cells. *ACS Nano* 2021;15:10597-608. DOI PubMed
136. Xiong T, Yu ZG, Wu H, et al. Defect engineering of oxygen-deficient manganese oxide to achieve high-performing aqueous Zinc ion battery. *Adv Energy Mater* 2019;9:1803815. DOI
137. Xiong T, Lee WSV, Xue J. K^+-intercalated MnO_2 electrode for high performance aqueous supercapacitor. *ACS Appl Energy Mater* 2018. DOI
138. Zhao Q, Song A, Zhao W, et al. Boosting the energy density of aqueous batteries via facile grotthuss proton transport. *Angew Chem Int Ed Engl* 2021;60:4169-74. DOI PubMed
139. Wang J, Sun X, Zhao H, et al. Superior-performance aqueous Zinc ion battery based on structural transformation of MnO_2 by rare earth doping. *J Phys Chem C* 2019;123:22735-41. DOI
140. Zhang Y, Deng S, Luo M, et al. Defect promoted capacity and durability of N-MnO_{2-x} branch arrays via low-temperature NH_3 treatment for advanced aqueous Zinc ion batteries. *Small* 2019;15:e1905452. DOI
141. Cai Y, Chua R, Huang S, Ren H, Srinivasan M. Amorphous manganese dioxide with the enhanced pseudocapacitive performance for aqueous rechargeable Zinc-ion battery. *Chem Eng J* 2020;396:125221. DOI
142. Chen X, Li W, Zeng Z, Reed D, Li X, Liu X. Engineering stable Zn-MnO_2 batteries by synergistic stabilization between the carbon nanofiber core and birnessite-MnO_2 nanosheets shell. *Chem Eng J* 2021;405:126969. DOI
143. Wu F, Gao X, Xu X, et al. MnO_2 nanosheet-assembled hollow polyhedron grown on carbon cloth for flexible aqueous Zinc-ion batteries. *ChemSusChem* 2020;13:1537-45. DOI PubMed
144. Long J, Yang F, Cuan J, et al. Boosted charge transfer in twinborn α-(Mn_2O_3-MnO_2) heterostructures: toward high-rate and ultralong-life Zinc-ion batteries. *ACS Appl Mater Interfaces* 2020;12:32526-35. DOI
145. Chen J, Cheng F. Combination of lightweight elements and nanostructured materials for batteries. *ACC Chem Res* 2009;42:713-23. DOI PubMed

146. Ling W, Wang P, Chen Z, et al. Nanostructure design strategies for aqueous Zinc-ion batteries. *ChemElectroChem* 2020;7:2957-78. DOI
147. Li D, Gao Q, Zhang H, et al. MnO_2 particles grown on the surface of N-doped hollow porous carbon nanospheres for aqueous rechargeable zinc ion batteries. *Appl Surf Sci* 2020;510:145458. DOI
148. Zhang X, Wu S, Deng S, et al. 3D CNTs networks enable MnO_2 cathodes with high capacity and superior rate capability for flexible rechargeable Zn-MnO_2 batteries. *Small Methods* 2019;3:1900525. DOI
149. Zhu X, Cao Z, Wang W, et al. Superior-performance aqueous zinc-ion batteries based on the in situ growth of MnO_2 nanosheets on V_2CT_x MXene. *ACS Nano* 2021;15:2971-83. DOI
150. Huang J, Tang X, Liu K, Fang G, He Z, Li Z. Interfacial chemical binding and improved kinetics assisting stable aqueous Zn-MnO_2 batteries. *Mater Today Energy* 2020;17:100475. DOI